Studies of Z boson decays to four leptons in pp collisions at $\sqrt{s} = 8$ TeV with the ATLAS detector at the LHC

Michael Anthony Baumer

of

Churchill College

A dissertation submitted to the University of Cambridge
for the degree of Master of Philosophy

Preface

While the Z boson is typically studied in dilepton final states, the rare $\mathrm{Z} \rightarrow \ell^+\ell^-\ell^+\ell^-$ decay mode allows the Z resonance to be studied in four-lepton final states as well. At the LHC, this process provides not only a test of radiative electroweak decays at high energy within the Standard Model, but also serves as a cross-check for measurements in the $\mathrm{H} \rightarrow \mathrm{ZZ}^{(*)} \rightarrow \ell^+\ell^-\ell^+\ell^-$ channel due to similarities in the four-lepton final states.

The first six chapters of this thesis present measurements of the fiducial and total cross-sections of the $pp \rightarrow \mathrm{Z} \rightarrow \ell^+\ell^-\ell^+\ell^-$ process ($\ell^\pm = \mathrm{e}^\pm, \mu^\pm$) in a phase space defined by $80 < M_{4\ell} < 100$ GeV and $M_{\ell^+\ell^-} \geq 4$ GeV for all same-flavour opposite-sign lepton pairs. These measurements are then used to infer the branching ratio of the Z boson to 4 leptons, $BR(\mathrm{Z} \rightarrow \ell^+\ell^-\ell^+\ell^-)$.

The final two chapters discuss the motivation for and the issues that arise in extending the phase space to include $M_{\ell^+\ell^-} \geq 1$ GeV, with preliminary cross-section results presented. In this extended phase space, analytical fits to the $\mathrm{Z} \rightarrow \ell^+\ell^-\ell^+\ell^-$ peak are performed to cross-check mass measurements of the recently discovered Higgs boson made in the $\mathrm{H} \rightarrow \mathrm{ZZ}^{(*)} \rightarrow \ell^+\ell^-\ell^+\ell^-$ channel.

Declaration

This dissertation is the result of my own work, except where explicit reference is made to the work of others, and has not been submitted for another qualification to this or any other university. This dissertation does not exceed the word limit for the Degree Committee for the Faculty of Physics and Chemistry.

M. A. Baumer

Acknowledgements

From conception to proofreading, I have been lucky to have the wonderful support of my supervisor, Dr. Richard Batley. Richard's eye for simplicity within the complex has been immensely helpful during this past year.

I owe much to my officemate Will Buttinger for his constant help in fixing bugs and improving my analysis skills. My code, based on his AnalysisCam framework, would have quickly become an unsalvageable mess without his patient advice.

None of this work would have been possible without generous funding from the Gates-Cambridge Trust. The Gates community has certainly been a highlight of my year here in Cambridge, and I am deeply grateful to have been a part of it.

I am also indebted to Prof. Andy Parker, who answered a cold call from me about joining the group two years ago and encouraged me to apply for the Gates scholarship. He was also responsible for securing travel funding for me to visit CERN this past spring, and ensured I was well-supported within the Cambridge HEP group.

My greatest debt is, of course, owed to my parents—for everything they've done to allow me to ride life's train so far in these 22 years. Without their loving nagging, this thesis never would have been written, and moreover, this entire year never would have happened, since my half-finished Gates application would still be lying on my desk, unsubmitted.

Abstract

This thesis presents measurements of the fiducial and total cross-section of the $\mathrm{Z} \rightarrow \ell^+\ell^-\ell^+\ell^-$ process ($\ell^\pm = \mathrm{e}^\pm, \mu^\pm$) at $\sqrt{s} = 8$ TeV using the ATLAS 2012 dataset ($\mathcal{L} = 20.3\ \mathrm{fb}^{-1}$). This process provides a practical cross-check of detector response to a four-lepton resonance in a regime similar to that of the newly discovered Higgs boson in the $\mathrm{H} \rightarrow \mathrm{ZZ}^{(*)} \rightarrow \ell^+\ell^-\ell^+\ell^-$ channel. The total $\mathrm{Z} \rightarrow \ell^+\ell^-\ell^+\ell^-$ cross-section in a phase space defined by 80 GeV $< M_{4\ell} <$ 100 GeV and $M_{\ell^+\ell^-} \geq 4$ GeV is measured as $\sigma_{\mathrm{PS}} = 149 \pm 15$ (stat.) $\pm$ 15 (syst.) $\pm$ 4 (lumi.) fb. The branching ratio, $BR(\mathrm{Z} \rightarrow \ell^+\ell^-\ell^+\ell^-)$, is measured as $(4.6 \pm 0.6) \times 10^{-6}$, which agrees with the Standard Model prediction of $(4.50 \pm 0.03) \times 10^{-6}$. A proposal for extending the phase space is presented and assessed, and analytical fits to the $\mathrm{Z} \rightarrow \ell^+\ell^-\ell^+\ell^-$ peak in this extended regime are presented.

Contents

Chapter 1.

Introduction

The unprecedented energy and luminosity of proton collisions at the Large Hadron Collider (LHC) represent a fantastic opportunity to test the Standard Model of particle physics (SM) in an unexplored regime. As a foundation for such explorations, measurements of Z boson production are often used as a baseline to establish and verify detector calibrations for other physics analyses. These studies are typically performed in dilepton final states, since $\mathrm{Z} \to \ell^+\ell^-$ is the experimentally cleanest mode of Z decay. The Feynman diagram for this process is shown in Figure 1.1.

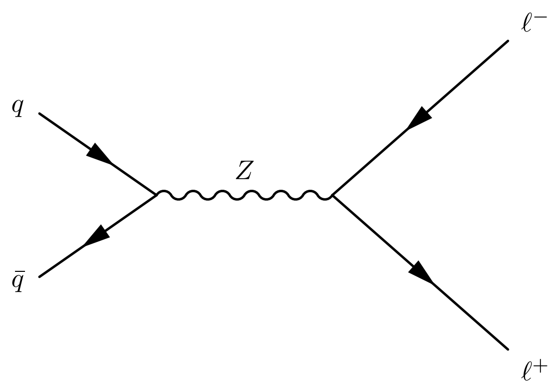

Figure 1.1.: A Feynman diagram illustrating the Z boson's two-lepton decay mode.

The ATLAS and CMS collaborations have both performed many studies of Z boson production (e.g. Refs. [1], [2]), as fundamental elements of prolific physics programmes which make precision measurements to test SM predictions in addition to searching for signs of new physics. Several of these searches have famously led to the recent discovery of a new particle consistent with the SM Higgs boson [3], [4].

The inspiration for much of the work contained in this thesis came from four-lepton mass spectra measured in $\mathrm{H} \to \mathrm{ZZ}^{(*)} \to \ell^+\ell^-\ell^+\ell^-$ analyses by both ATLAS and CMS.

Figure 1.2 shows the summary plots from the ATLAS and CMS papers announcing the discovery of the Higgs boson, which both show a four-lepton resonance peaked at $M_Z \approx 91$ GeV to the left of the new Higgs resonance around 125 GeV. This resonance appears due to a rare decay mode of the Z boson, $Z \to \ell^+\ell^-\ell^+\ell^-$, whose Feynman diagram is shown in Figure 1.3.

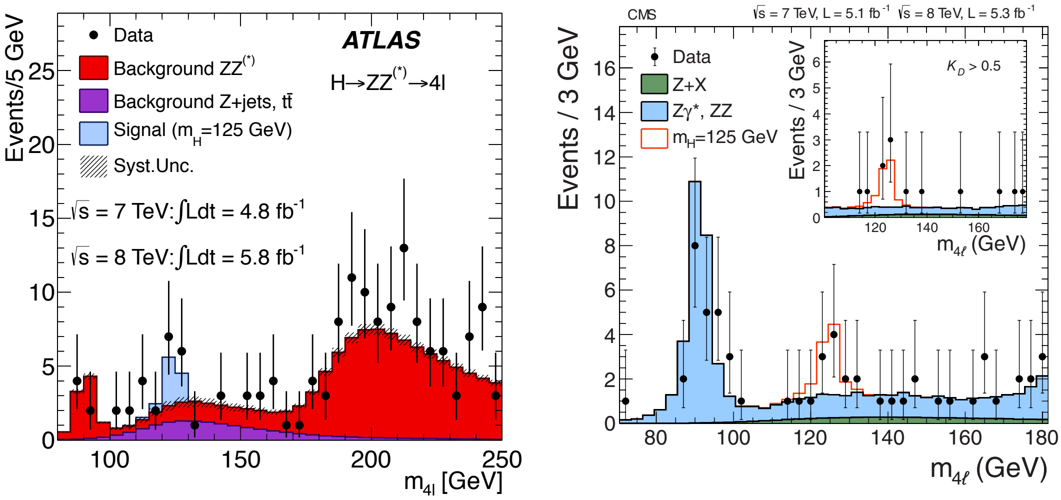

Figure 1.2.: Four-lepton mass spectra from the ATLAS (left) and CMS (right) Higgs boson discovery papers [3], [4], both showing a resonant peak around $M_Z \approx 91$ GeV. The most recent updated versions of these plots, which include more data and therefore show a more pronounced effect, can be found in Refs. [5] and [6].

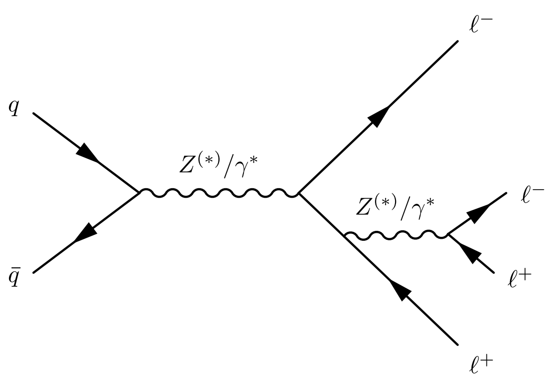

Figure 1.3.: Feynman diagram for the rare $Z \to \ell^+\ell^-\ell^+\ell^-$ decay mode, which is the main subject of this thesis.

These observations motivated the creation of an ATLAS working group dedicated to characterising the $Z \to \ell^+\ell^-\ell^+\ell^-$ resonance. Much of the work presented in this thesis was performed as a member of this analysis team. The primary goal of the analysis was to measure fiducial and total cross-sections for the $Z \to \ell^+\ell^-\ell^+\ell^-$ process in a phase space defined by

$$80 \text{ GeV} < M_{4\ell} < 100 \text{ GeV};\ M_{\ell^+\ell^-} > 4 \text{ GeV}, \tag{1.1}$$

where $M_{\ell^+\ell^-} \geq 4$ GeV represents a minimum dilepton mass requirement for all same-flavour opposite-sign lepton pairs.

The most recent results from this group are documented in [7]. Work adapted from this analysis forms the bulk of the first six chapters of this thesis.

The CMS collaboration has measured the $\mathrm{Z} \to \ell^+\ell^-\ell^+\ell^-$ cross-section and branching ratio in $\sqrt{s} = 7$ TeV data [8], using a phase space identical to the one defined above. Since this thesis deals exclusively with $\sqrt{s} = 8$ TeV data, the cross-section results presented within are not directly comparable to those from CMS. However, although cross-section measurements depend on $\sqrt{s}$, branching ratio measurements are independent of the collision centre-of-mass energy. Therefore, the measurement of the $\mathrm{Z} \to \ell^+\ell^-\ell^+\ell^-$ branching ratio made in this thesis will be comparable to the CMS measurement, given in Ref. [8] as $BR(\mathrm{Z} \to \ell^+\ell^-\ell^+\ell^-) = (4.2^{+0.9}_{-0.8}\ (\text{stat.}) \pm 0.2\ (\text{syst.})) \times 10^{-6}$.

The latter half of this thesis discusses the motivation for extending the phase space to include $\mathrm{Z} \to \ell^+\ell^-\ell^+\ell^-$ decays with lower $M_{\ell^+\ell^-}$, and the issues encountered in simulating $\mathrm{Z} \to \ell^+\ell^-\ell^+\ell^-$ decays at low dilepton mass. In spite of simulation difficulties, preliminary cross-section measurements in an extended phase space defined by $80 < M_{4\ell} < 100$ GeV; $M_{\ell^+\ell^-} \geq 1$ GeV are presented. Finally, analytical fits to the $\mathrm{Z} \to \ell^+\ell^-\ell^+\ell^-$ resonance peak are performed and used to validate the accuracy of four-lepton mass scale, as a cross-check for mass measurements of the newly observed Higgs resonance, observed in the kinematically similar $\mathrm{H} \to \mathrm{ZZ}^{(*)} \to \ell^+\ell^-\ell^+\ell^-$ channel around $M_{4\ell} \approx 125$ GeV.

Chapter 2.

Theory

Figure 2.1 shows the two leading-order Feynman diagrams for four lepton production via two intermediate $Z^{(*)}/\gamma^*$ propagators. Both of these diagrams can be considered as channels of a general process denoted as $Z^{(*)}Z^{(*)} \to \ell^+\ell^-\ell^+\ell^-$.

In the s-channel diagram, two leptons are produced via a $Z^{(*)}/\gamma^*$, one of which radiates two more leptons via a second $Z^{(*)}/\gamma^*$, resulting in four final-state leptons whose total invariant mass is the mass of the initial $Z^{(*)}/\gamma^*$. This contributes to a resonant peak when the initial particle is an on-shell Z.

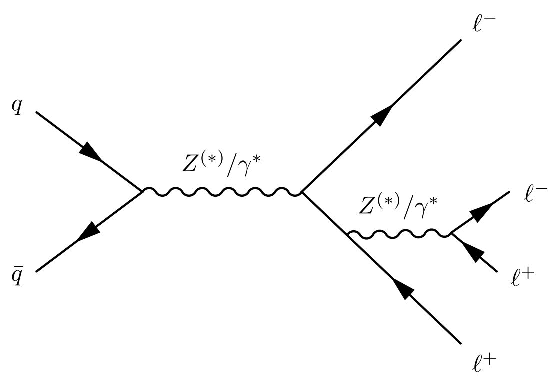

(a) s-channel

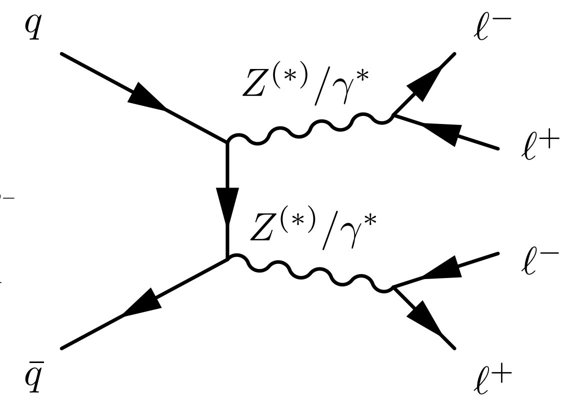

(b) t-channel

Figure 2.1.: Feynman diagrams illustrating s-channel and t-channel $Z^{(*)}Z^{(*)} \to \ell^+\ell^-\ell^+\ell^-$ production.

Similarly, the t-channel diagram illustrates the production of four leptons via two intermediate $Z^{(*)}/\gamma^*$ particles. However, in this case, the four-lepton invariant mass is a continuum with no resonant peak, similar to that produced by the SM $ZZ \to \ell^+\ell^-\ell^+\ell^-$ process where one or both Z bosons are on-shell [9].

In this thesis, the general process to which both of these diagrams contribute will be denoted $Z^{(*)}Z^{(*)} \to \ell^+\ell^-\ell^+\ell^-$. When this process is restricted to the four-lepton mass range of 80 GeV $< M_{4\ell} <$ 100 GeV, the region where the s-channel diagram is dominant (see Figure 2.2), it will be referred to as $Z \to \ell^+\ell^-\ell^+\ell^-$. The fiducial and phase-space cross-sections measured in this thesis will include both the s- and t-channels together. However, for the measurement of $BR(Z \to \ell^+\ell^-\ell^+\ell^-)$, the contribution of t-channel diagrams will be subtracted. In a mass window of 80 GeV $< M_{4\ell} <$ 100 GeV, this contribution is estimated using MC simulations to be 4% in the $4e$ and 4μ channels and 4.5% in the mixed-flavour ($2e2\mu$) channels.

This difference between the same- and mixed-flavour channels is due to exchange interference. In the mixed-flavour channels, the four final-state leptons (e^-, e^+, μ^-, μ^+) are all distinguishable. However, in the same-flavour final state ($\mu^-, \mu^+, \mu^-, \mu^+$), the two μ^- and μ^+ are indistinguishable, causing additional interfering diagrams to contribute to the cross-section.

Gluon-gluon fusion processes also contribute to $Z^{(*)}Z^{(*)} \to \ell^+\ell^-\ell^+\ell^-$ production. However, as shown in Figure 2.3, such diagrams necessarily involve at least one quark loop, and are therefore suppressed compared to quark-initiated $Z^{(*)}Z^{(*)} \to \ell^+\ell^-\ell^+\ell^-$, which can occur at tree level. In the range of 80 GeV $< M_{4\ell} <$ 100 GeV, the contribution of these gluon diagrams is negligible.

Table 2.1 presents a summary of theoretical predictions relevant to this analysis. Calculations are performed using the POWHEG BOX generator [10], which implements the POWHEG method [11], [12] to compute expected SM cross-sections at next-to-leading order. Expected cross-sections in the phase space, for both the inclusive process and the t-channel alone, are shown, along with an NLO prediction for inclusive $\sigma(pp \to Z)$, which will be necessary for computing $BR(Z \to \ell^+\ell^-\ell^+\ell^-)$.

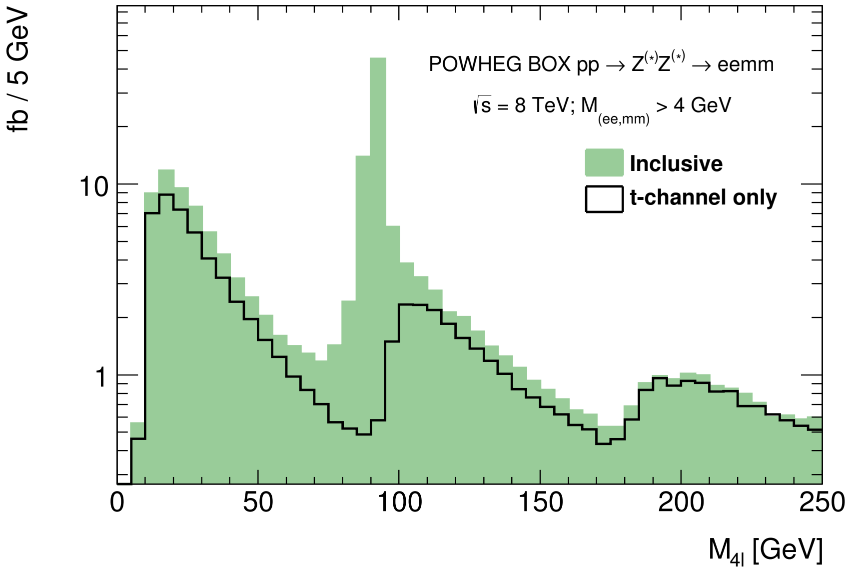

Figure 2.2.: Generator-level four-lepton mass spectrum calculated by POWHEG, showing both the inclusive spectrum and the t-channel component of the $Z^{(*)}Z^{(*)} \to \ell^+\ell^-\ell^+\ell^-$ process.

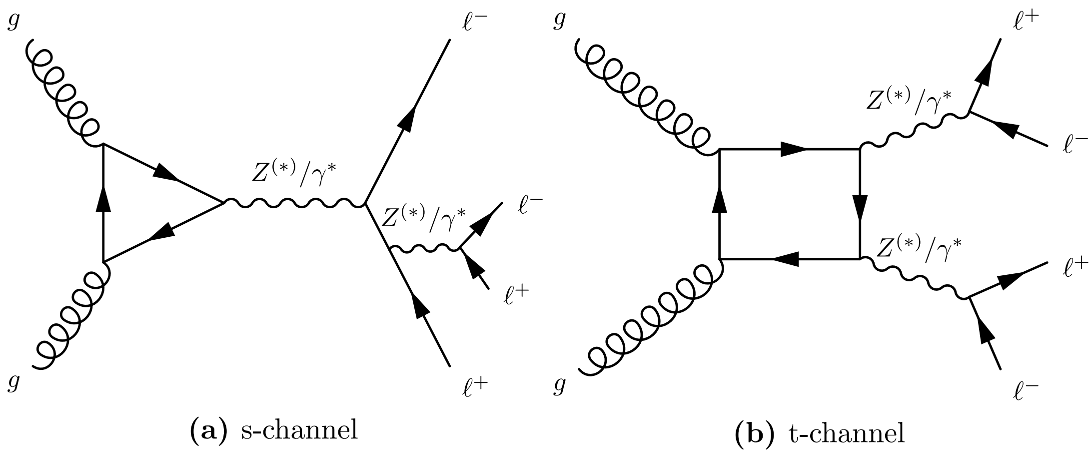

Figure 2.3.: Feynman diagrams of gluon-initiated s-channel (left) and t-channel (right) $Z^{(*)}Z^{(*)} \to \ell^+\ell^-\ell^+\ell^-$. Because these processes involve quark loops, they are suppressed with respect to the quark-initiated diagrams shown in Figure 2.1.

Table 2.1.: Summary of theoretical predictions relevant to this analysis. SM expectations for the $Z^{(*)}Z^{(*)} \to \ell^+\ell^-\ell^+\ell^-$ process are computed for the phase space defined by 80 GeV $< M_{4\ell} <$ 100 GeV and $M_{\ell^+\ell^-} >$ 4 GeV.

Quantity	Expected Value
$\sigma_{\mathrm{PS}}(\mathrm{pp} \to Z^{(*)}Z^{(*)} \to 4e + 4\mu)$	72.6 ± 0.3 fb
$\sigma_{\mathrm{PS}}(\mathrm{pp} \to Z^{(*)}Z^{(*)} \to 2e2\mu)$	69.5 ± 0.2 fb
$\sigma_{\mathrm{PS}}(\mathrm{pp} \to Z^{(*)}Z^{(*)} \to 4\ell)$	142.2 ± 0.4 fb
t-channel: $\mathrm{pp} \to Z^{(*)}Z^{(*)} \to 4e + 4\mu$	3.0 ± 0.1 fb
t-channel: $\mathrm{pp} \to Z^{(*)}Z^{(*)} \to 2e2\mu$	3.1 ± 0.1 fb
t-channel: $\mathrm{pp} \to Z^{(*)}Z^{(*)} \to 4\ell$	6.1 ± 0.2 fb
Inclusive $\sigma(\mathrm{pp} \to Z)$	30.3 ± 0.8 nb
$BR(Z \to \ell^+\ell^-\ell^+\ell^-)$	$(4.5 \pm 0.03) \times 10^{-6}$

Chapter 3.

The ATLAS Experiment at CERN

ATLAS (**A** **T**oroidal **L**HC **A**pparatu**S**) is the largest of the four major experiments at the LHC designed to test the SM and search for new physics. Along with CMS (**C**ompact **M**uon **S**olenoid), ATLAS is one of two 'general-purpose' detectors, designed to be sensitive to a wide range of both known and possible new physics. A schematic overview of ATLAS is shown in Figure 3.1, with two human figures superimposed above the beamline between two muon end-cap wheels at left for scale.

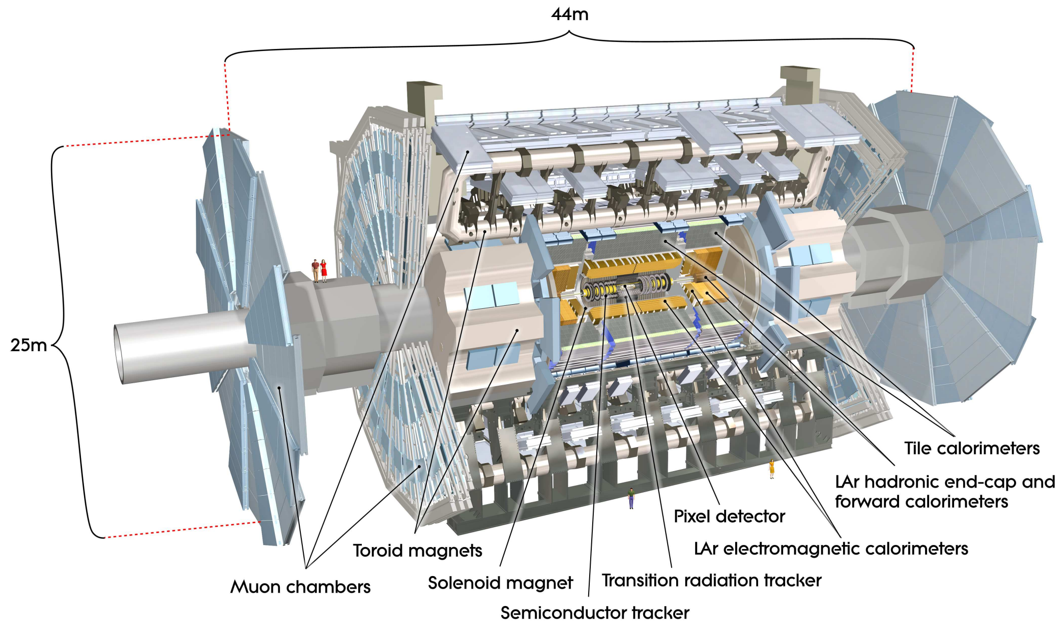

Figure 3.1.: A diagram of the ATLAS detector with various detector subsystems labelled.

Two antiparallel beams of protons enter from opposite sides along the detector's axis, (nominally) colliding at the exact centre of the detector. The ATLAS coordinate system takes this nominal interaction point as its origin, with the z-axis pointing along the beamline. A right-handed coordinate system is established by specifying the x-axis as pointing to the nominal centre of the LHC ring, and the y-axis as pointing upwards, perpendicular to the plane of the accelerator.

From this system, a more useful cylindrical coordinate system can be derived in the following way. The angle θ, defined as an object's angular displacement from the z-axis, is used to calculate the pseudorapidity $\eta = -\ln\left[\tan\left(\theta/2\right)\right]$. The azimuth ϕ is measured in the plane transverse to the beamline with the x-axis defining $\phi = 0$. Separation between objects in this (η, ϕ) space is calculated as $\Delta R = \sqrt{(\Delta\eta)^2 + (\Delta\phi)^2}$.

Another important quantity, transverse momentum (denoted p_T), is the magnitude of the the projection of a particle's momentum ($\vec{p}$) into the transverse ($\theta = 90°$) plane, calculated as $p_T = |\vec{p}| \,/\cosh\eta$. At hadron colliders, p_T is often a more useful quantity than $|p|$. Parton distribution functions (PDFs), which determine the fractional momentum carried by each constituent parton, make the initial longitudinal momentum in the hard scatter almost unconstrained. In any head-on collision, however, initial transverse momentum is always zero. Therefore, the transverse momenta of all final state particles must always balance to zero to conserve momentum.

3.1. The Large Hadron Collider

The Large Hadron Collider (LHC) is a circular accelerator 27 km in circumference, designed to collide proton beams at eventual energies of 7 TeV per beam [13]. At the time of writing, it is the world's premier hadron collider, its current pp collision energy of $\sqrt{s} = 8$ TeV surpassing that of Fermilab's Tevatron, which at the time of its shutdown in 2011 had achieved $p\overline{p}$ collisions at $\sqrt{s} = 1.96$ TeV.

A schematic of the accelerator, including the locations of each of the four primary experiments along the beamline, is shown in Figure 3.2. It was constructed using superconducting magnets placed into a circular tunnel previously built for the Large Electron-Positron Collider (LEP). Many other CERN assets were also repurposed for the LHC, including the Super Proton Synchrotron (SPS), which now serves as a booster ring for the LHC, injecting 450 GeV protons into the LHC ring during fills.

In addition to high energy, the LHC was also designed for high luminosity. With a design target for peak luminosity set at 10^{34} cm^{-2}s^{-1}, the LHC has already achieved

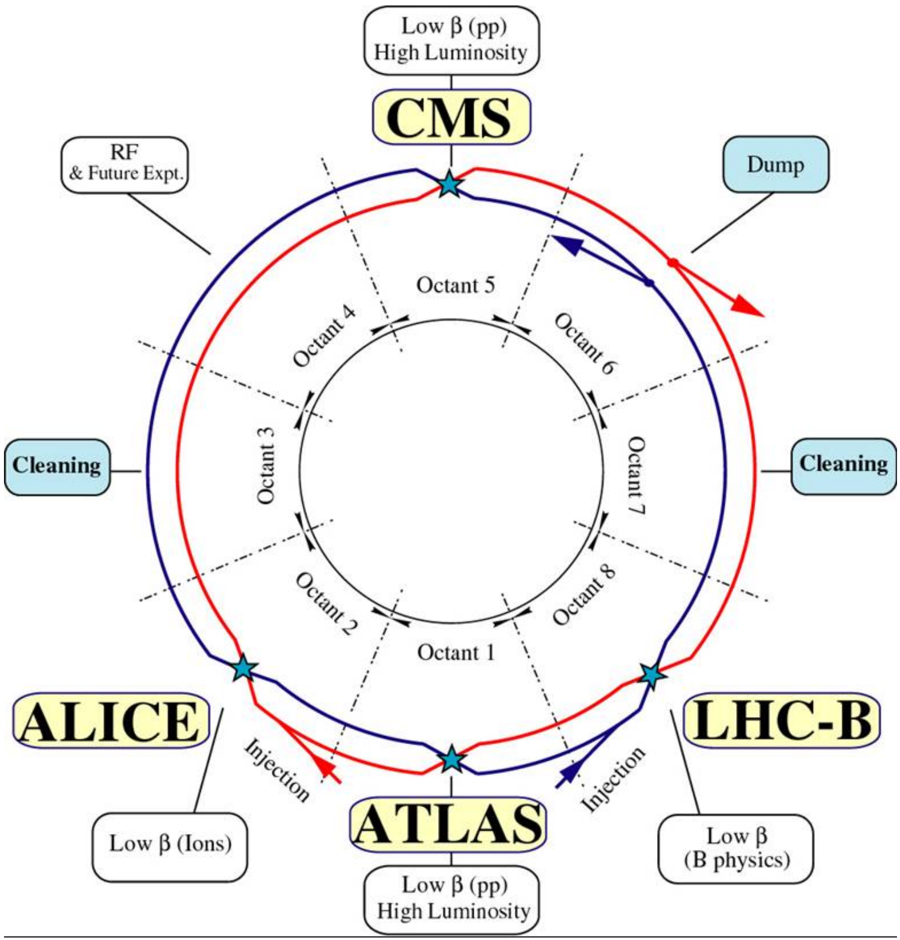

Figure 3.2.: A schematic of LHC beam crossings with the locations of the four main experiments indicated. Adapted from Ref. [13].

a peak luminosity greater than 7×10^{33} cm^{-2}s^{-1}. In 2012, this high luminosity was achieved by counter-circulating 1380 bunches of 1.48×10^{11} protons, spaced in time by 50 ns. This results in a collision rate of 20 million bunch crossings per second. Managing this rapid collision rate is challenging; methods of coping with such data-taking conditions are described later in this thesis.

3.2. Overview of the ATLAS Detector

The ATLAS detector, described in detail in Ref. [14], is composed of many subsystems. These include the inner detector (ID) for tracking, electromagnetic and hadronic calorimeters (ECAL and HCAL, respectively), and the muon spectrometer (MS), with triggering hardware embedded throughout the detector. In this section, the detector subsystems relevant to measuring Z $\rightarrow \ell^+\ell^-\ell^+\ell^-$ final states—the ID, ECAL, and MS—are described.

The inner detector provides tracking and vertexing information for all charged particles with $p_T > 0.5$ GeV and consists of three main subcomponents [15]. From the interaction point outwards, these are the pixel detector, the semiconductor tracker (SCT), and the transition radiation tracker (TRT). Together, these components provide full tracking coverage within a pseudorapidity range of $|\eta| < 2.5$. The entire ID is immersed in a 2 T solenoidal magnetic field, making momentum measurements from transverse track curvature possible for both electrons and muons. Measurements of track impact parameters are made by extrapolating ID tracks back to the primary vertex. The transverse impact parameter, d_0, is defined as the projection of a line marking a track's closest approach to the primary vertex into the transverse plane. The longitudinal impact parameter, z_0, is the difference in z coordinate between the point used to determine d_0 and the primary vertex.

The near-hermetic ATLAS ECAL is centred around precision liquid-argon (LAr) calorimeters interspersed with lead absorbers in the region $|\eta| < 2.5$ [16]. Overlapping and extending the coverage of the LAr barrel is the electromagnetic end-cap calorimeter (EMEC), which instruments the $1.375 < |\eta| < 3.2$ region. The forward calorimeter (FCal) provides coverage at even higher pseudorapidity, from $3.1 < |\eta| < 4.9$. Fine granularity is crucial to the efficiency of electron reconstruction identification, so the LAr barrel calorimeters feature an inner layer with cells of dimension $\Delta\eta \times \Delta\phi = 0.0031 \times 0.025$. This segmentation is fine enough to distinguish photons produced in π^0 decays. The middle layer, which captures most of the electromagnetic energy of an incoming electron, has a granularity of $\Delta\eta \times \Delta\phi = 0.025 \times 0.025$.

The muon spectrometer (MS), physically the largest ATLAS sub-detector, is integrated into the toroidal magnet system and forms the outer layer of the detector [17]. The magnets create a toroidal magnetic field of 0.5-1 T within the MS which bends muons in the sagittal (η) plane. Muon momenta are measured by three layers of detectors called Monitored Drift Tubes (MDTs), each of which uses hits from three to eight layers of drift tubes to measure a 'tracklet' within the MS layer. Tracklets from each of the three MDT layers are combined to form a full MS track. Coverage of the MDTs extends out to $|\eta| < 2.7$, excepting a small gap around $\eta \approx 0$, which provides space for services to the ID and calorimeters and accommodates the detector's feet and other support structures. This gap varies in size with ϕ in the range of $|\eta| <$ 0.04-0.08.

The ATLAS calorimeter systems and the MS contain specialised hardware to allow for fast and efficient triggering on interesting events, such as those producing high-p_T leptons. Triggering is necessary for data-taking at ATLAS; given that the collision rate is 20 MHz, it is impossible to read out and record the events from every bunch crossing. In practice, the rate of events being written out to disk must be kept to $\approx$ 200 Hz [18].

This is achieved using a three layer triggering system described in Ref. [19]. The Level 1 (L1) trigger uses hardware-based processing and coarse selection to reduce the event rate to $\approx$ 75 kHz. The Level 2 (L2) and Event Filter (EF) triggers are both software-based, with L1 seeding L2, which in turn seeds the EF level. The three trigger layers provide increasingly fine selections (since each layer is allotted more time for processing than the layer that seeds it), reducing the event rate to a manageable level [20], [21].

Chapter 4.

Data and Monte Carlo Simulation

4.1. Signal and Background MC Simulations

In this thesis, Monte Carlo (MC) simulation is used to model both signal and background processes. Production of MC samples begins by using specialised event generators to create a sample of matrix elements for a specified process of interest.

The POWHEG BOX generator, described earlier in Chapter 2, is used to perform next-to-leading order simulations of the $\mathrm{Z}^{(*)}\mathrm{Z}^{(*)} \rightarrow \ell^+\ell^-\ell^+\ell^-$ process [22]. The primary input parameter in the POWHEG generation process is known as `mllmin`. The value of this parameter represents the minimum mass of any same-flavour opposite-sign pair allowed to be created by the generator. This parameter is central to the extensions of the phase space discussed in Chapter 7, and is therefore introduced here. For now, POWHEG signal samples are generated with `mllmin` = 4 GeV. The Sherpa generator [23], which performs calculations at leading order (LO), is used to produce a sample of $\mathrm{Z}^{(*)}\mathrm{Z}^{(*)} \rightarrow \ell^+\ell^-\ell^+\ell^-$ events to use for cross-checks.

For the $Z+$jets background, Alpgen [24] is used to simulate the production of single Z bosons in association with both light and heavy jets. MC@NLO [25] is used to simulate $\mathrm{t\bar{t}}$ production, and POWHEG is used to generate a $\mathrm{W}^{\pm}\mathrm{Z}$ background sample. For all signal and background samples where $\tau^{\pm}$ leptons are produced, their decays are calculated with the TAUOLA library [26], [27].

The four-vectors produced in event generation become inputs to programmes that add electromagnetic showering effects such as initial and final state radiation. These effects are calculated using Photos [28] and Photos++ [29], which despite their differing implementations have comparable physics content. Sherpa has an internal showering functionality that is used for the samples produced with the Sherpa generator.

Further specialised programmes are used to model hadronic showering effects which hadronise any colour-charged particles generated by the hard scatter or underlying event (bare quarks, gluons), showering them into more stable colourless particles (baryons, mesons). For this procedure, Pythia8 [30] is used with the POWHEG samples, Jimmy [31] for Alpgen and MC@NLO, and Sherpa's internal showering functionality for its samples. Details of MC sample production are given in Table 4.1.

Table 4.1.: Summary of MC samples used in this analysis.

Process	Generator	EM Shower	Hadronic Shower	Order	PDF Set
Signal $Z \to 4\ell$	PowHeg	Photos++	Pythia8	NLO	CTEQ10
Signal $Z \to 4\ell$	Sherpa	Sherpa	Sherpa	LO	CTEQ10
Z + light jets	Alpgen	Photos	Jimmy	LO	CTEQ 6L1
Z + heavy flavour	Alpgen	Photos	Jimmy	LO	CTEQ 6L1
$t\bar{t}$	MC@NLO	Photos	Jimmy	NLO	CTEQ10
WZ	PowHeg	Photos++	Pythia8	NLO	CTEQ10

All MC simulations use either CTEQ 6L1 [32] or CTEQ 10 [33] parton distribution functions (PDFs) to model how momentum is divided between the valence quarks, sea quarks, and gluons within a proton. Collective soft QCD effects are modelled with underlying event parameters tuned for ATLAS as described in [34].

The expected response of the ATLAS detector to MC events is simulated using a detailed model of the detector [35] based on GEANT4 [36]. After detector simulation, object reconstruction and identification algorithms are applied as for real data. Analysis selection can now be applied to MC simulated events in the same way it is applied to real data. A cartoon illustrating the interface between data analysis and MC simulation is shown in Figure 4.1.

The detector simulation is necessarily an imperfect model of the ATLAS detector. Deviations observed in the alignments of different detector subsystems and improvements in understanding of the detector from performance studies mean that the simulation fails to accurately represent the performance parameters of the actual detector. To account

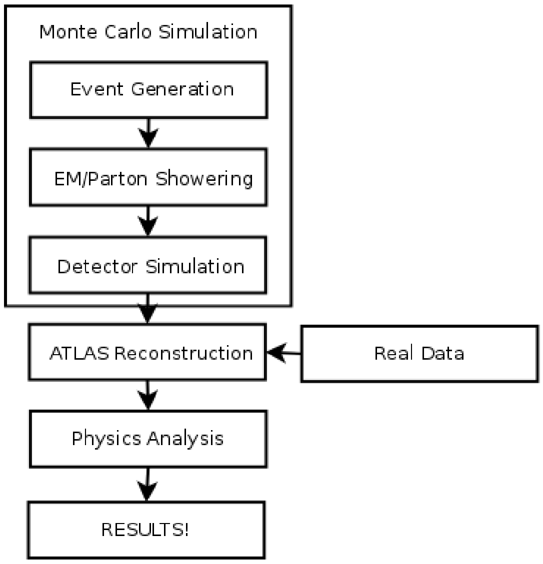

Figure 4.1.: A diagram of MC production and use within ATLAS.

for this, samples of MC events are tuned by applying various corrections and scale factors to bring them into closer agreement with real performance data.

These corrections include muon and electron smearing (event-by-event Gaussian blurring of lepton p_T distributions) to bring the simulated and observed momentum resolutions into agreement. Scale factors are used to correct disagreements between data and MC simulation in efficiencies of various procedures such as triggering on one or more leptons, lepton reconstruction, and lepton identification. All distributions shown in this thesis have such corrections applied to all constituent MC samples. Systematic uncertainties arising from these corrections are discussed in Section 6.3.

4.2. ATLAS Data-taking Conditions in 2012

Between the 2011 and 2012 ATLAS data-taking runs, two improvements were made that extended the physics reach of 2012 analyses. Firstly, the LHC beam energy was increased from 3.5 TeV to 4 TeV, thereby increasing the centre-of-mass energy of the collisions from 7 TeV to 8 TeV. These higher energies increased the the cross-section of Z $\rightarrow \ell^+\ell^-\ell^+\ell^-$ by 16.5% for the 2012 run. The second improvement was an increase in instantaneous luminosity achieved by increasing the density of the colliding proton bunches. This allowed ATLAS to collect integrated luminosity more rapidly over the course of the data-taking period, by the end resulting in a dataset four times larger than that recorded in 2011.

One challenge associated with the increased luminosity was a corresponding increase in pileup. Higher bunch densities caused more interactions to occur during the same bunch crossing, resulting in the products of many distinct interactions overlapping inside the detector. Figure 4.2 illustrates the increase in μ, the average number of interactions per bunch crossing, between 2011 and 2012. This effect makes the reconstruction and identification of physics objects more challenging. In addition, since MC samples are produced with a fixed set of pileup conditions, they do not necessarily mimic the pileup conditions eventually observed in the data. Instead of re-simulating every MC sample to mirror the observed pileup, each is reweighted to match the pileup conditions observed in data.

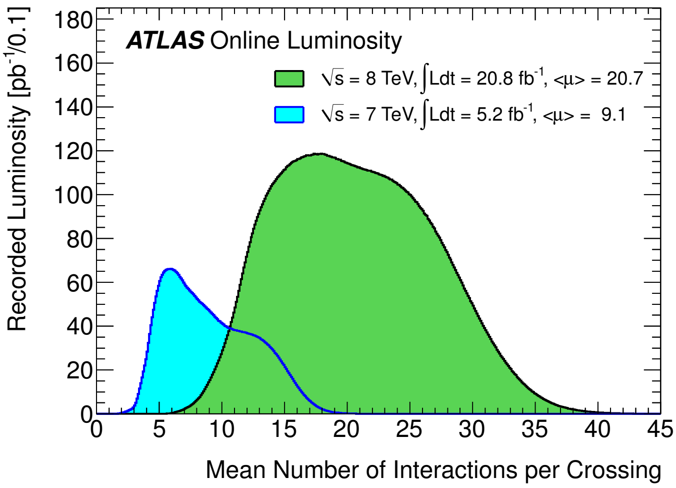

Figure 4.2.: Comparison of 2011 and 2012 pileup conditions, adapted from Ref. [37]. The yearly average number of interactions per bunch crossing, $\langle\mu\rangle$, is given in the legend for both runs.

During 2012, the LHC delivered $\sqrt{s} = 8$ TeV proton-proton collisions corresponding to a total integrated luminosity of $\mathcal{L} = 23.3$ fb^{-1}. Of these, a dataset corresponding to 21.7 fb^{-1} was recorded by the ATLAS detector. This inefficiency is primarily due to delays between the declaration of stable beam conditions by the LHC team and the full activation of sensitive ATLAS components.

During data-taking operations, detector condition databases record any transient or chronic malfunctions in detector subsystems [38]. Data recorded during instances of critical subsystem failures are rejected by means of a GoodRunsList (GRL) [39]. For the 2012 ATLAS dataset, rejecting data recorded during a period in which the detector is determined to be unsuitable for physics data-taking leaves a dataset corresponding to a total integrated luminosity of 20.3 fb^{-1}. This dataset is the starting point for the analysis described in the following chapter.

Chapter 5.

Physics Object and Event Selection

5.1. Electron Selection

Electrons are reconstructed using a 'sliding window' algorithm [40] which uses a mask of size $\Delta\eta \times \Delta\phi = (3 \times 0.025) \times (5 \times 0.025)$ to identify clusters of energy deposits in the electromagnetic calorimeter. These clusters are then matched to charged tracks refitted using the GSF algorithm [41] to account for bremsstrahlung losses in the ID. The efficient performance of these algorithms has been validated in Ref. [42].

In the past, cut-based electron identification algorithms have been used for all ATLAS analyses. More recently, however, a likelihood-based neural network (hereafter referred to as LikelihoodID) has been developed that uses a wide range of reconstruction variables to compute a likelihood discriminant. Electrons are selected by cutting on the value of this discriminant. The value of this cut, which varies with the number of reconstructed vertices to minimise pileup-dependence (improving on the old cut-based identification), determines the signal efficiency and background rejection. There are five standard operating points (`VeryLoose`, `Loose`, `Medium`, `Tight`, and `VeryTight`); `Loose` is chosen because it offers the same signal efficiency as the previous cut-based identification algorithm, with improved background rejection.

To limit electron acceptance to the η range where the ID provides full tracking coverage (see Section 3.2), electrons are required to have $|\eta| < 2.47$. Since reconstruction and identification algorithms have been validated only in a limited phase space, all electrons must have $E_T > 7$ GeV. E_T is defined as

$$E_T = \frac{E_{\text{cluster}}}{\cosh(\eta_{\text{track}})}, \tag{5.1}$$

where E_{cluster} is the electron energy as measured by the ECAL and η_{track} is the pseudorapidity as measured by the electron's refitted ID track.

Electrons falling into any regions of the detector suffering from localised quality issues, such as dead or insufficient high-voltage supply, dead front-end boards, or isolated noisy channels are rejected. Furthermore, an electron's extrapolated track may be displaced no more than 10 mm along the beamline ($|z_0| < 10$ mm) to reject electrons not associated with the primary vertex.

5.2. Muon Selection

Compared to electrons, muons have a much cleaner signal: the magnet surrounding the inner detector bends muons in the transverse plane, allowing the ID to measure their momentum. The toroidal magnetic field surrounding the MS then bends their paths in the sagittal plane, where the muon system makes a completely independent momentum measurement by combining up to three tracklets from the MDT layers into an MS track.

Because muons offer such a clean signal in the detector, four categories of muons (Combined, Segment-Tagged, StandAlone, and Calo-Tagged) are defined to extend acceptance in this sector as much as possible. The detection profiles of these four types are illustrated in Figure 5.1. The first three of these categories use the STACO identification algorithm, while the fourth uses a dedicated CaloTag algorithm [43], [44]. The high lepton multiplicity of the $Z \rightarrow \ell^+\ell^-\ell^+\ell^-$ signal implies that even small improvements in muon acceptance can significantly improve the overall acceptance of four-lepton events, especially in the high-resolution 4μ channel [45].

Combined muons are the purest [46] identification category. These muons are identified when a complete MS track (constructed from hits in all three MDT layers) is extrapolated back to a matching ID track and combined via a weighted average into one measurement.

Segment-tagged muons recover efficiency for (usually low-p_T) muons that register a tracklet only in the innermost MS layer, making it difficult to extract a momentum measurement from the MS. If this tracklet can be extrapolated back to an isolated ID track, then this combination is identified as a segment-tagged muon. ID measurements are used to require all muons in these two categories to have $|z_0| < 10$ mm, and $d_0 < 1$ mm, to help reject cosmic rays. In addition, both combined and segment-tagged muons are required to have $p_T > 4$ GeV and $|\eta| < 2.7$. The p_T is limited by the phase space of performance validation studies, and the η limit is constrained by MDT coverage within the MS, as described in Section 3.2. However, in practice, given that ID tracking coverage ends at $\eta = \pm 2.5$, the number of combined and segment-tagged muons falls off sharply between $2.5 < |\eta| < 2.7$.

StandAlone muons recover acceptance for muons in this high-η region. They are reconstructed from a full (3-layer) MS track alone, which has no corresponding ID track. Since muons are expected to leave an ID track if they fall in the region where the ID provides tracking coverage, acceptance of StandAlone muons (with $p_T > 4$ GeV) is limited to the high-η region ($2.5 < |\eta| < 2.7$).

The final category of muons, calo-tagged muons, recovers acceptance in the physical gap in the MS around $\eta \approx 0$ described in Section 3.2. Since the previous three categories rely on information from the muon spectrometer for identification, they fail to identify muons which fall in this MS coverage gap. Efficiency at $\eta \approx 0$ is regained using the principle that, as minimally-ionising particles, muons deposit small amounts of energy as they traverse the ATLAS calorimeter system. The CaloTag identification algorithm combines ID tracks with low-energy calorimeter deposits that have slowly falling dE/dx profiles to identify calo-tagged muons in the region $|\eta| < 0.1$. Because this method relies on the calorimeter rather than ID and MS tracking exclusively, it gives a less pure sample of muon candidates than the other categories, especially at low p_T. Calo-tagged muons are therefore required to have $p_T > 15$ GeV. As in the case of combined and segment-tagged muons, ID tracking information is used to require $|z_0| < 10$ mm and $d_0 < 1$ mm for all calo-tagged muons.

A summary of all object selection requirements for both electrons and muons is given in Table 5.1.

5.3. Lepton Overlap Removal

Reconstruction and identification of physics objects is hindered by the heavy pileup conditions of the LHC's 2012 run, described in Section 4.2. When the signatures of

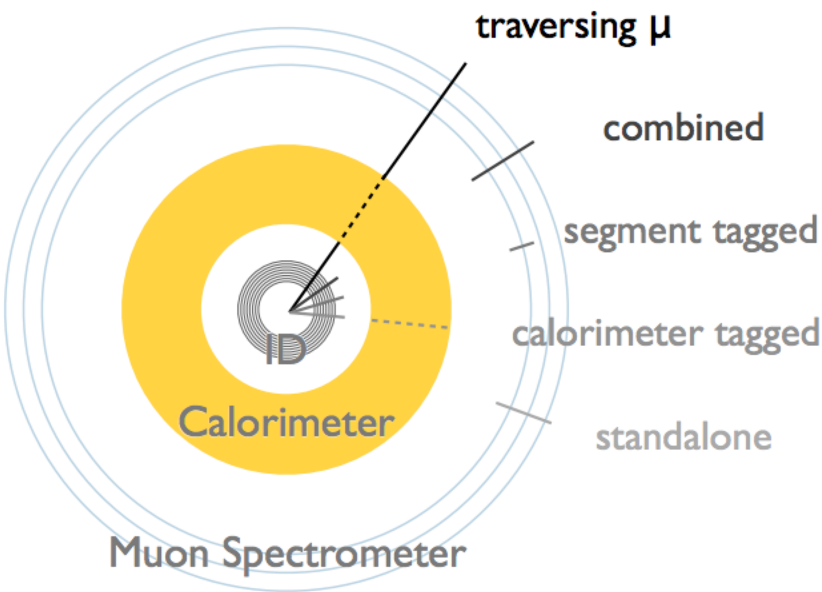

Figure 5.1.: Diagram illustrating the detector signatures of the four categories of muons used in this analysis. Adapted from Ref. [47]

Table 5.1.: A summary of electron and muon selection requirements.

Electrons		
Pass LikelihoodID		
$E_T > 7$ GeV; $\lvert\eta_{cluster}\rvert < 2.47$		
No quality defects		
$\lvert z_0\rvert < 10$ mm		
Muons		
Combined + Segment-Tagged	StandAlone	Calo-Tagged
STACO algorithm	STACO algorithm	CaloTag algorithm
$p_T > 4$ GeV	$p_T > 4$ GeV	$p_T > 15$ GeV
$\lvert\eta\rvert < 2.7$	$2.5 < \lvert\eta\rvert < 2.7$	$\lvert\eta\rvert < 0.1$
Track quality cuts*	≥ 1 hit in all 3 MS layers	Track quality cuts*
$\lvert z_0\rvert < 10$ mm		$\lvert z_0\rvert < 10$ mm
$d_0 < 1$ mm		$d_0 < 1$ mm

*See Appendix A for details

particles overlap in the various detector subsystems, it becomes difficult to reconstruct object and event properties accurately. For a high lepton multiplicity signal like $Z \rightarrow \ell^+\ell^-\ell^+\ell^-$, it is necessary to reject leptons that were likely mis-measured due to overlap with other objects.

Overlap of electron pairs is handled at both the ID and ECAL level. In the ID, if two electrons share the same track (defined as $\Delta R_{track} < 0.02$), the electron with the highest $E_T^{cluster}$, the E_T as measured by the electromagnetic calorimeter, is retained. Overlap at the calorimeter level is governed by the granularity of the ECAL (see Section 3.2) and the size of the 'sliding window' used for electron reconstruction (see Section 5.1). If two electron candidates are closer in η than $|\Delta\eta| < 3 \times 0.025$ and separated in ϕ by less than $|\Delta\phi| < 5 \times 0.025$, only the electron with the higher $E_T^{cluster}$ is retained.

Lastly, any electron sharing an ID track with a STACO muon candidate is removed, to reject cases in which an ID track is matched to both an electromagnetic calorimeter shower and an MS track. Electrons, rather than muons, are removed in such cases because it is easier for a muon to mimic an electron by losing energy on its way through the calorimeter system than it is for an electron to punch through the entire calorimeter and register hits in the MS.

The muon selection detailed in Section 5.2 extends beyond high-purity STACO combined muons to increase overall muon acceptance, but selects extension muons of varying types and qualities. To prevent double counting of muons at low $|\eta|$, any muons from CaloTag that fall within $\Delta R_{track} < 0.1$ of a muon from STACO are rejected. This ensures that if a single low-η muon is reconstructed by two different algorithms, the muon from the higher-purity reconstruction algorithm is accepted.

Secondly, since both electrons and calo-tagged muons rely on ID tracks and calorimeter deposits for reconstruction, any calo-tagged muon that shares an ID track with an electron ($\Delta R_{track} < 0.02$) is rejected to prevent ID and ECAL deposits coming from a single particle from being reconstructed as multiple physics objects.

Lastly, any StandAlone muon that falls within $\Delta R < 0.2$ of a segment-tagged muon is rejected. StandAlone muons are reconstructed from MS tracks which fail to be matched with an ID track, while segment-tagged muons are the combination of an ID track with an inner layer MS tracklet. Observing these two types near each other in an event indicates an increased probability that a single muon's detector signatures failed to be combined properly, resulting in the double counting of single high-η muons.

5.4. Event Selection

Because the motivation for this analysis came from $H \to ZZ^{(*)} \to \ell^+\ell^-\ell^+\ell^-$ measurements, this analysis for $Z \to \ell^+\ell^-\ell^+\ell^-$ attempts to follow the current $H \to ZZ^{(*)} \to \ell^+\ell^-\ell^+\ell^-$ selection described in Ref. [48], as closely as possible, deviating only in ways that significantly increase acceptance for the single Z resonance.

On top of the baseline quality cuts required by the GRL, events recorded in coincidence with calorimeter noise spikes, or corrupted on disk during dataset production are rejected. The only additional preselection required is that events have at least one reconstructed primary vertex with at least 3 associated tracks.

For triggering, a range of unprescaled single and di-lepton triggers, described in Table 5.2, is used. All trigger decisions are computed at the Event Filter (EF) level, seeded by upstream L1 and L2 triggers as described in Section 3.2. The main content of each trigger name is the trigger threshold level, given in GeV as the numbers following 'e' and 'mu'.The rest of each name encodes technical information about the trigger configuration.

Table 5.2.: ATLAS trigger setup used for 2012 data.

Type	Trigger Name
Single Electron	`e24vhi_medium1`
	`e60_medium1`
Single Muon	`mu24i_tight`
	`mu36_tight`
Di-Electron	`2e12Tvh_loose1`
Di-Muon	`2mu13`
	`mu18_tight_mu8_EFFS`
Electron-Muon	`e12Tvh_medium1_mu8`
	`e24vhi_loose1_mu8`

Once an event passes one of the triggers, it is required to contain *at least* four muons, four electrons, or two of each flavour of lepton, where all four leptons pass their respective object selection requirements, outlined in Sections 5.1 to 5.3.

Candidate quadruplets are then assembled out of all (possibly more than four) selected leptons in the event according to the following rules:

- A quadruplet is composed of a pairing of two same-flavour opposite-sign (SFOS) lepton pairs.
- At most one StandAlone/calo-tagged muon is allowed per quadruplet.
- Within a quadruplet, the SFOS dilepton whose mass is closest to M_Z is considered the *primary dilepton*. The other is referred to as the *secondary dilepton*.

If no valid quadruplet can be formed, the event is rejected. The analysis can now be separated into four distinct channels: 4e, 2e2μ, 2μ2e, and 4μ. For the mixed-flavour channels, the flavour of the primary dilepton is written first.

For each quadruplet, the leading and subleading leptons are required to have $p_T >$ 20 GeV and 15 GeV, respectively, in order to have sufficiently hard objects for reliable triggering. If the third leading lepton is an electron, it must have $p_T > 10$ GeV; if a muon, the requirement is relaxed to $p_T > 8$ GeV. In order to increase overall acceptance, however, the fourth leading lepton may have p_T as low as its respective object selection threshold ($p_T > 7$ GeV for electrons, 4 GeV for muons). Additionally, at least one object (or pair of objects, in the case of dilepton triggers) must be 'trigger-matched,' i.e. identified as the object that caused one of the triggers listed in Table 5.2 to fire.

In these first two stages, multiple possible quadruplets per event are considered. If a quadruplet fails any of the preceding cuts, that particular quadruplet is rejected, but other valid quadruplets in the event continue to be considered. For the purposes of making cutflow tables, an event receives an entry at the 'Kinematics' and 'Trigger Matching' stages if at least one of its quadruplets passes the cut, but no more than one entry is made per event.

If, after these selections, more than one candidate quadruplet remains, exactly one is chosen by first selecting quadruplets whose primary dilepton minimises $|M_{12} - M_Z|$, and then, if two quadruplets share a primary dilepton, choosing the quadruplet with the highest-mass secondary dilepton (largest M_{34}). This single quadruplet continues through the analysis selection as described below. However, if it fails any of the cuts that follow, the entire event is rejected.

The quadruplet's primary dilepton mass must satisfy $M_{12} > 20$ GeV. Given that the quadruplet selection procedure prioritises the mass of the primary dilepton, events where M_{12} is large and M_{34} is small are preferentially selected over events where the two are more well-balanced. Therefore, the cut on the secondary dilepton mass M_{34} has a large effect on acceptance, since the M_{34} distribution is peaked at low dilepton mass. Later in

Table 5.3.: Summary of Z $\rightarrow \ell^+\ell^-\ell^+\ell^-$Event Selection

Category	Selection Details
Kinematics	$p_T^{\text{lead}} > 20$ GeV, $p_T^{\text{sublead}} > 15$ GeV
	$p_T^{\text{3rd}} > 10$ GeV for electrons; $p_T^{\text{3rd}} > 8$ GeV for muons
Trigger Matching	At least one lepton (or dilepton) matched to a trigger object
Selection of 1 quadruplet	Select quadruplet with primary dilepton mass (M_{12}) closest to M_Z,
	then highest secondary dilepton mass (M_{34})
Primary Dilepton Mass	$M_{12} > 20$ GeV
Secondary Dilepton Mass	$M_{34} > 5$ GeV
Lepton separation	$\Delta R(\ell, \ell') > 0.1$ if same flavour
	$\Delta R(\ell, \ell') > 0.2$ if opposite flavour
J/ψ veto	$M_{\ell^+\ell^-} > 5$ GeV for SFOS lepton pairs
Track Isolation	Adjusted $\sum p_T$ of nearby tracks $< 15\%$ of lepton p_T for all leptons in quadruplet
Calorimeter Isolation	Adjusted $\sum E_T$ of nearby calorimeter deposits: $< 20\%$ of electron E_T
	$< 30\%$ of muon p_T for combined, segment-tagged, and calo-tagged muons
	$< 15\%$ of muon p_T for all StandAlone muons
Impact Parameter Significance	$\lvert d_0/\sigma(d_0)\rvert < 3.5$ for all muons
	$\lvert d_0/\sigma(d_0)\rvert < 6.5$ for all electrons
Z Mass Window	80 GeV $< M_{4\ell} <$ 100 GeV

this thesis, looser versions of this requirement are considered, but for now the lower limit is chosen as $M_{34} > 5$ GeV.

The purpose of the overlap removal components of the object selection described in Section 5.3 was to prevent the double-counting of overlapping lepton candidates. However, since a lepton's measurements can still be contaminated by close-by but non-overlapping objects, lepton separation requirements are imposed at the event selection level. Leptons within the quadruplet must be separated in (η, ϕ) space by at least $\Delta R \geq 0.1$ radians from other leptons of the same flavour and $\Delta R \geq 0.2$ radians from leptons of opposite flavour.

A J/ψ veto is applied by requiring the mass of all possible SFOS dileptons constructed from members of the quadruplet to be greater than 5 GeV. This cut also restricts the analysis to the phase space modelled by the primary POWHEG signal samples, produced with `mllmin` = 4 GeV.

To mitigate the effects of pileup as discussed in Section 4.2 and to suppress non-prompt lepton backgrounds, each of the leptons in the quadruplet is required to be isolated both in the ID and in the ECAL. The ID (track) isolation is computed by first summing p_T contributions from all other track components within a cone defined by $\Delta R_{\text{track}} < 0.2$ around each quadruplet lepton. This Σp_T is then adjusted by subtracting the p_T of any other quadruplet leptons falling within the $\Delta R_{\text{track}} < 0.2$ cone. The adjusted Σp_T is required to be less than 15% of a lepton's p_T for both electrons and muons.

ECAL isolation is calculated similarly, with summation taking place over the E_T of calorimeter deposits falling within a $\Delta R < 0.2$ cone instead of nearby tracks. This isolation sum is adjusted by subtracting the E_T of any quadruplet electron within a cone defined by $\Delta R < 0.18$ around the lepton. The cone size of 0.18 is chosen to account for the intrinsic width of ECAL showers from which electrons are reconstructed. Muon contributions to ECAL isolation are negligible.

The adjusted ΣE_T is required to be lower than 30% of muon p_T for all muon types except StandAlone muons, where a limit of 15% of p_T is imposed. For electrons the adjusted summation is required to be less than 20% of electron E_T.

To ensure that the tracks of the four leptons comprising the Z candidate are consistent with having a common origin, a requirement is placed on the ratio $|d_0/\sigma(d_0)|$, the significance (in units of σ) of the deviation of an object's impact parameter from the nominal value of zero. $|d_0/\sigma(d_0)| < 6.5$ is required for all electrons from the quadruplet, while all muons must satisfy $|d_0/\sigma(d_0)| < 3.5$.

The final analysis selection is a window imposed around the Z mass of 80 GeV $< M_{4\ell} <$ 100 GeV.

Chapter 6.

Results

6.1. Background Estimation

Many ATLAS analyses, particularly those searching for new physics, target small signals obscured by large backgrounds. In the case of $Z \rightarrow \ell^+\ell^-\ell^+\ell^-$, despite its low cross-section, it dominates all background processes in signal region. This is because the only SM process that produces two same-flavour opposite-sign pairs of prompt leptons is $Z^{(*)}Z^{(*)}$ production. For other processes to contribute to the signal region requires that they produce 2 or 3 prompt leptons with 2 or 1 additional non-prompt leptons, respectively. Isolation requirements such as those described in Section 5.4 restrict acceptance of non-prompt leptons, so processes such as $W^{\pm}Z$, $t\bar{t}$, and $Z + \text{jets}$ contribute little background in the $Z \rightarrow \ell^+\ell^-\ell^+\ell^-$signal region.

Low background acceptance means that some MC samples have very few events passing the analysis selection, resulting in large statistical errors on the corresponding MC background estimation. In such cases, producing MC samples with sufficient statistics to accurately model the contributions of all backgrounds would require massive simulation and reconstruction efforts, and is therefore not practicable.

In light of these limitations, many analyses instead leverage the large amounts of data ATLAS has amassed thus far by selecting a subset of data that mirrors the characteristics of a target background, creating 'data-driven' background samples. These samples not only scale in size with the ATLAS dataset, but also reduce dependence on sometimes-unreliable MC simulations. Data-driven samples have been created to estimate background contributions to $Z \rightarrow \ell^+\ell^-\ell^+\ell^-$ from $Z + \text{jets}$ and $t\bar{t}$ processes, using a method described in Section 5 of Ref. [7]. In this thesis, however, MC simulations will be used for all background estimates. The conclusion of both of these methods—using data-driven estimates for $Z + \text{jets}$ and $t\bar{t}$ with MC estimates for all other processes, and using MC estimates for all backgrounds—is that backgrounds are small ($\approx 1\%$ of data) in the signal region.

A combined cutflow for $Z + \text{jets}$, $t\bar{t}$, $W^{\pm}Z$ and $\tau^{\pm}$ channels of the $Z \to \ell^+\ell^-\ell^+\ell^-$ signal process is given in Table 6.1. This shows that the analysis requirements most important for suppressing non-prompt lepton backgrounds are the track and calorimeter isolation requirements and the impact parameter cut.

Table 6.2 presents a summary of background contributions, broken down by channel and process. For processes where no events from within the corresponding MC samples were selected in certain channels, the background contribution is listed as zero. Estimates from the data-driven methods described in Ref. [7] verify the small contributions of each background process to the signal region.

Table 6.1.: Combined cutflow for all MC background samples, normalised to $\mathcal{L} = 20.3$ fb^{-1}.

	$4e$	$2e2\mu$	$2\mu 2e$	4μ
$\geq$ 4 leptons	146.3	5303.2	5303.2	5956.3
4 SFOS leptons	86.8	2755.7	334.0	3574.7
Kinematics	50.6	1586.2	223.5	1980.3
Trigger Matched	50.5	1581.7	222.6	1973.5
M_{12}	48.1	1488.2	180.2	1916.5
M_{34}	40.8	624.6	169.8	1003.9
Object Separation	40.6	584.4	145.0	840.9
J/ψ veto	36.7	584.4	145.0	681.0
Track Isolation	11.0	45.5	16.1	44.0
Calorimeter Isolation	9.1	31.3	11.2	25.3
Impact Parameter	8.6	20.9	9.6	14.4
Z Mass Window	0.13	0.38	0.42	0.46

Table 6.2.: Summary of background estimates from MC simulations, normalised to $\mathcal{L} = 20.3$ fb^{-1}. Equivalent integrated luminosities of the MC samples used for the estimations are given in the far-right column. Values appearing as zero in this table due to limited MC statistics are verified to be small using the data-driven method described in Ref. [7].

	$4e$	$2e2\mu$	$2\mu 2e$	4μ	MC Equivalent $\int \mathcal{L}\, dt$
Z + light jets	0	0	0	0	~ 10 fb^{-1}
Z + heavy flavour	0.004	0.12	0.01	0.04	~ 5000 fb^{-1}
$t\bar{t}$	0	0	0.25	0	~ 100 fb^{-1}
τ channels	0.07	0.20	0.17	0.42	~ 5000 fb^{-1}
$W^{\pm}Z$	0.06	0.07	0	0	~ 500 fb^{-1}
Total MC Background	0.13	0.38	0.42	0.46	

6.2. Comparisons of Data and MC simulations

Tables 6.3 and 6.4 give cutflow breakdowns of the analysis selection as applied to ATLAS data as well as POWHEG signal MC samples. The latter confirms that the analysis selection accepts signal events with high efficiency, while the the data cutflow produces results that agree with MC simulation inside the Z mass window. In total, 147 $Z \to \ell^+\ell^-\ell^+\ell^-$ candidates were observed in the ATLAS 2012 dataset, when 142.2 were expected.

Several plots are included to demonstrate both shape and normalisation agreement between data and a sum of MC signal and background samples, both channel-by-channel and inclusively, for several key event variables. All distributions are plotted for events within 80 GeV $< M_{4\ell} <$ 100 GeV, except for the four-lepton mass spectra, where this requirement is omitted to allow measurements of the sidebands of the $Z \to \ell^+\ell^-\ell^+\ell^-$ resonance. Figure 6.1 shows inclusive plots of the p_T of the four leptons comprising the quadruplet, ordered by p_T. Figure 6.2 shows distributions of the mass of the primary dilepton (M_{12}); Figure 6.3 contains plots of the mass of the secondary dilepton (M_{34}).

Figure 6.4 illustrates a resonance peaking around M_Z in the four-lepton mass spectra of all four channels (and by extension, in the inclusive channel). In the side-bands of this resonance, few events are observed. This confirms that non-resonant backgrounds in the signal region are small.

Table 6.3.: $Z \rightarrow \ell^+\ell^-\ell^+\ell^-$ cutflow selection for ATLAS 2012 data.

	$4e$	$2e2\mu$	$2\mu 2e$	4μ
4 SFOS leptons	423	7650	3001	46629
Kinematics	284	3137	1128	12137
Trigger Matched	283	3111	1117	11696
M_{12}	282	2736	902	10853
M_{34}	220	1364	706	7382
Object Separation	218	1109	552	3943
J/ψ veto	183	1109	552	1830
Track Isolation	125	269	163	354
Calo Isolation	103	236	144	313
Impact Parameter	100	192	137	272
Z Mass Window	16	47	15	69

Table 6.4.: Cutflow table indicating the number of events from POWHEG signal samples passing each stage of selection, normalised to $\mathcal{L} = 20.3$ fb^{-1}.

	$4e$	$2e2\mu$	$2\mu 2e$	4μ
≥ 4 leptons	116.1	382.7	382.7	298.6
4 SFOS leptons	111.6	224.1	151.0	295.9
Kinematics	103.2	188.9	138.1	249.1
Trigger Matched	103.2	188.8	138.0	249.1
M_{12}	98.6	177.7	130.6	242.2
M_{34}	94.6	160.9	122.4	224.9
Object Separation	94.6	156.1	119.3	224.0
J/ψ veto	92.4	156.1	119.3	216.6
Track Isolation	89.5	147.8	115.2	205.1
Calo Isolation	83.9	139.8	109.0	197.3
Impact Parameter	82.2	136.9	106.9	194.3
Z Mass Window	14.67	41.92	19.03	65.15

Figure 6.5 shows the separation ΔR between the constituent leptons of both the primary and secondary dileptons, illustrating the correlation between dilepton mass and separation. The primary dilepton's distribution has a pronounced peak around $\Delta R = \pi$, which indicates the back-to-back emission expected in a high-mass system. The secondary dilepton, in contrast, peaks at low ΔR, as expected for a low-mass dilepton.

6.3. Systematic Uncertainties

The systematic uncertainties for this analysis can be divided into four independent categories with varying degrees of correlation between analysis channels: statistical (fully uncorrelated), systematic (partially correlated), theoretical (partially correlated), and luminosity-related (fully correlated). Statistical uncertainties are straightforward to compute using standard Poisson statistics.

Estimating the uncertainty on the total integrated luminosity delivered by the LHC and observed by ATLAS requires online measurements of the instantaneous luminosity of collisions as they occur, measured by a specialised set of forward detectors (see Chapter 7 of Ref. [14] for details). Also required are dedicated measurements known as Van der Meer (VdM) scans [49], during which the two proton beams in the LHC are offset from one another, then slowly steered together, through to an opposite offset.

For the 2012 dataset, the uncertainty on the integrated luminosity is $\pm 2.8\%$. It is derived, following the same methodology as that detailed in Ref. [50], from a preliminary calibration of the luminosity scale derived from VdM scans performed in November 2012.

Theoretical uncertainties arise from the dependence of MC generators on arbitrary parameters, such as choice of PDF set and scale of renormalisation and factorisation. Estimates for these uncertainties are given in Section 4 of Ref. [7]. Calculated using POWHEG with varying input parameters, the total uncertainty on theoretical acceptance is estimated at $\approx 1.5\%$ in all four channels. Since statistical and experimental systematic uncertainties are the dominant sources of uncertainty in this analysis, theoretical uncertainties are neglected in this thesis.

Experimental systematic uncertainties are estimated by varying experimental parameters by $\pm 1\sigma$ and measuring the effect of this variation on the overall acceptance. Two types of experimental uncertainties are considered. The first are variations of object calibration scales, which vary the values of single-particle measurements such

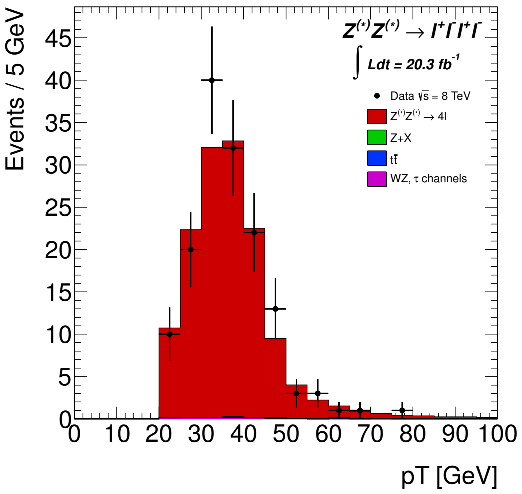

(a) Leading lepton

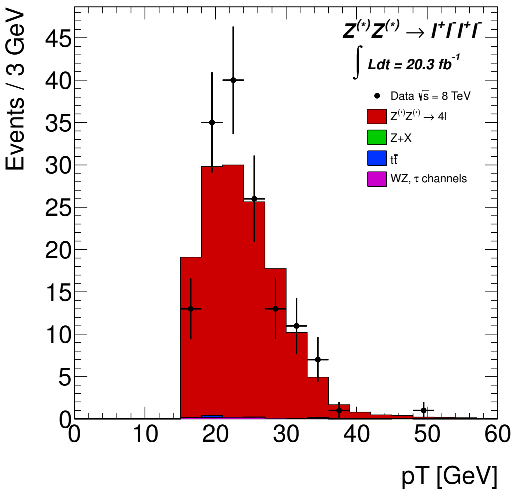

(b) Subleading lepton

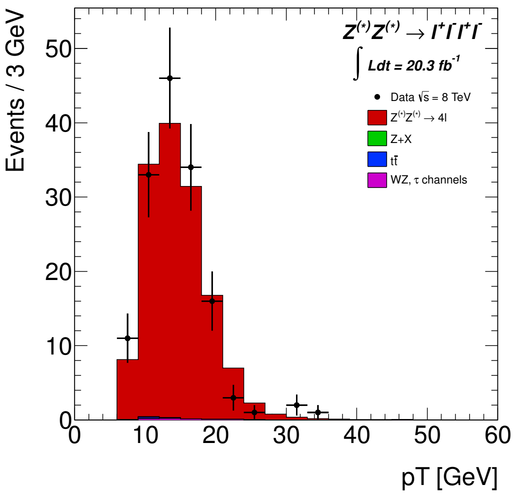

(c) Third leading lepton

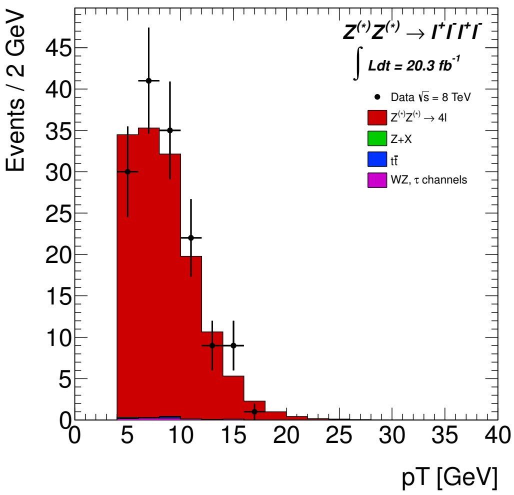

(d) Fourth leading lepton

Figure 6.1.: Transverse momentum distributions for the (p_T-ordered) leptons of the quadruplet. These distributions represent the sum of all four individual analysis channels (the 'inclusive channel').

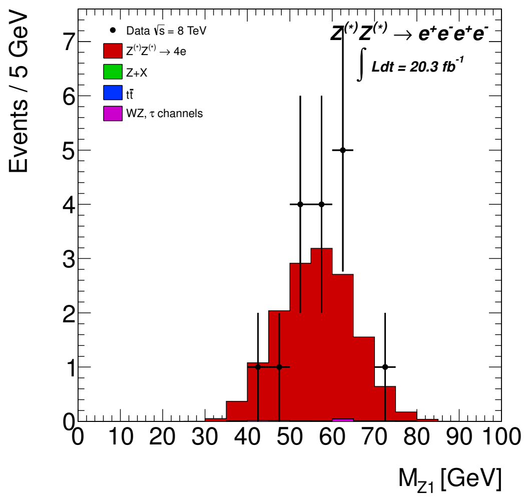

(a) 4e channel

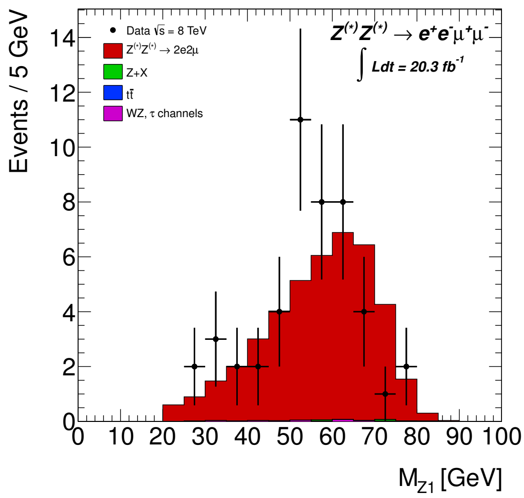

(b) 2e2μ channel

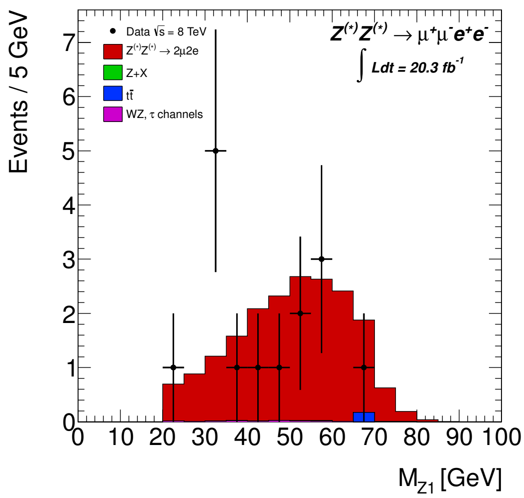

(c) 2μ2e channel

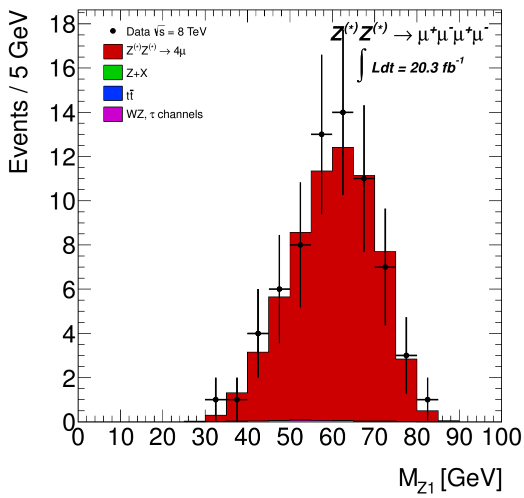

(d) 4μ channel

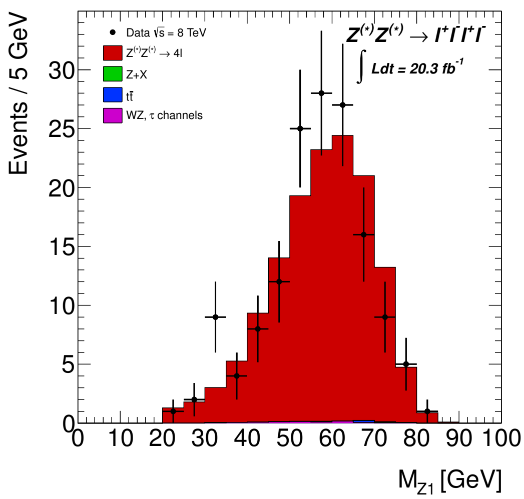

(e) Inclusive channel

Figure 6.2.: Distributions of the mass of the primary dilepton (M_{12}) for each individual channel, as well as the inclusive total of all four channels.

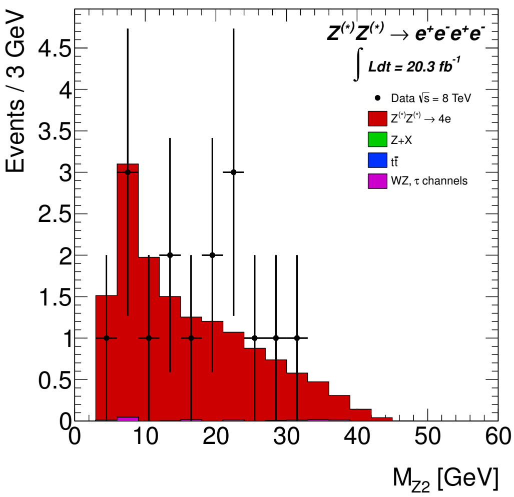

(a) $4e$ channel

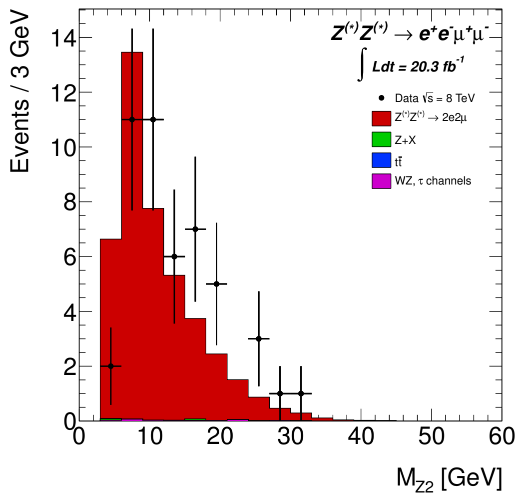

(b) $2e2\mu$ channel

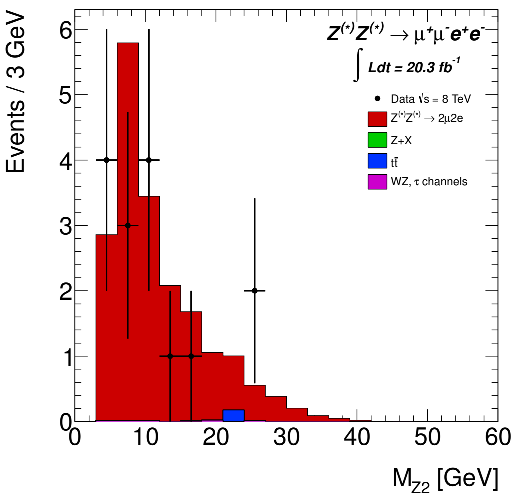

(c) $2\mu 2e$ channel

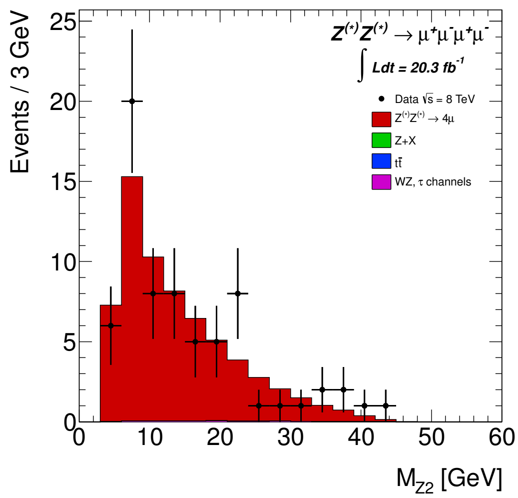

(d) 4μ channel

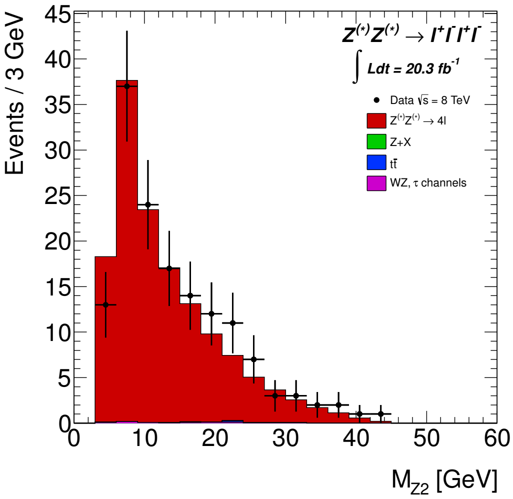

(e) Inclusive channel

Figure 6.3.: Distributions of the mass of the secondary dilepton (M_{34}) for each individual channel, as well as the inclusive channel.

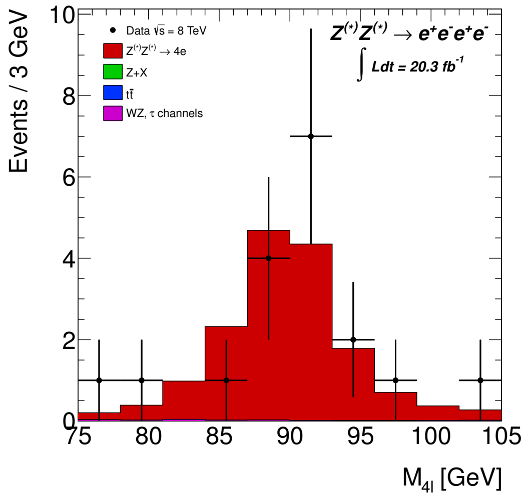

(a) 4e channel

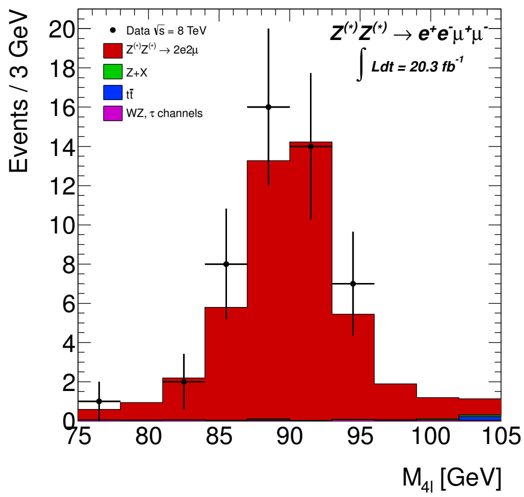

(b) 2e2μ channel

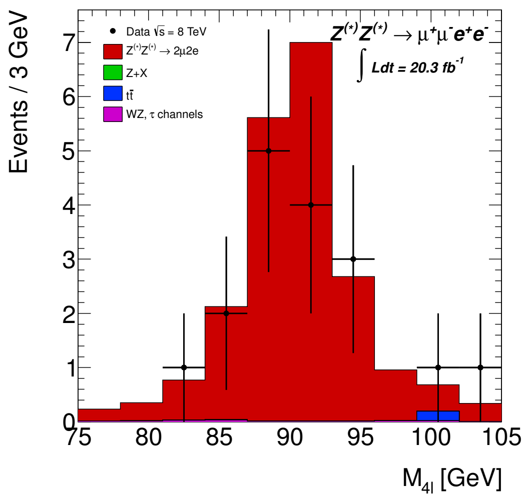

(c) 2μ2e channel

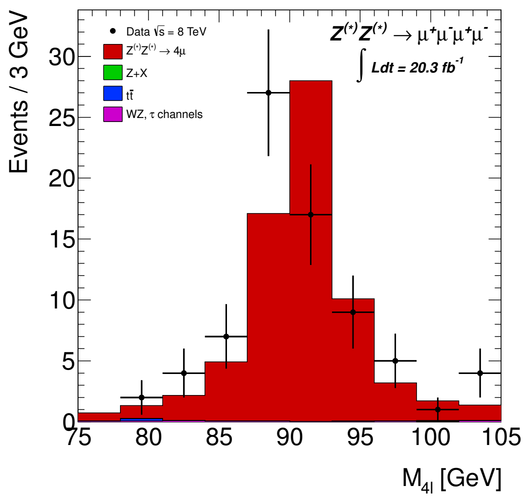

(d) 4μ channel

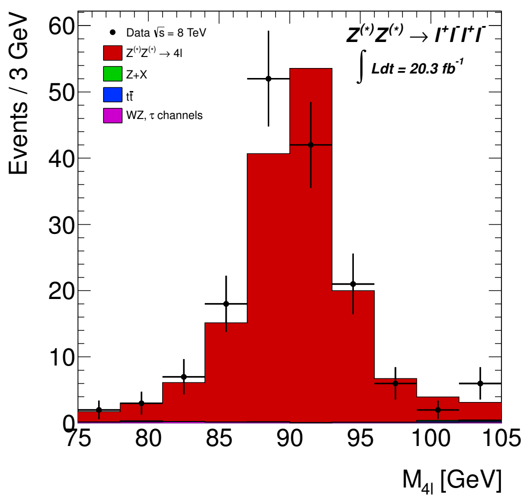

(e) Inclusive channel

Figure 6.4.: Four-lepton mass distributions plotted for each individual channel, as well as the inclusive channel. The near-absence of non-resonant background is supported by the observation of low-population side-bands in each channel.

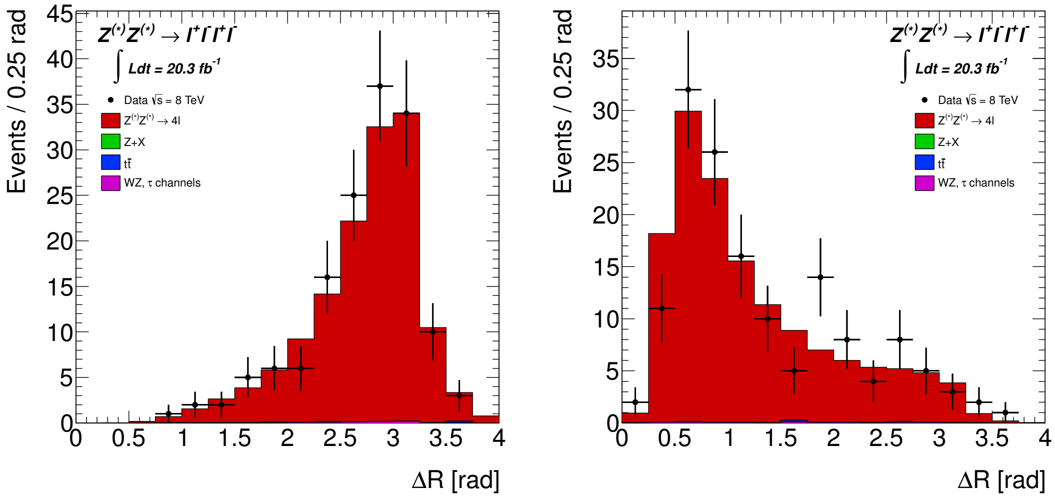

Figure 6.5.: Distributions of the separation of the leptons comprising the (left) primary dilepton and (right) secondary dilepton, plotted for the inclusive channel.

as p_T. These include electron and muon smearing variations, lepton energy resolution uncertainties, and lepton energy and momentum scales. The second are uncertainties on scale factors which are applied as event weights to correct MC distributions as described in Section 4.1. The uncertainties on these scale factors are found to be dominant over those from smearing and calibration scales. Neglecting these, the significant (scale factor) uncertainties are detailed in Table 6.5. All computed uncertainties are symmetric, and their total is obtained by adding each independent source of uncertainty in quadrature.

Table 6.5.: Summary of experimental systematic uncertainties.

	$4e$	$2e2\mu$	$2\mu 2e$	4μ
Electron Reconstruction	5.76%	1.80%	3.67%	—
Electron Identification	18.95%	4.87%	12.37%	—
Muon Identification	—	0.06%	0.06%	0.11%
Lepton Trigger	0.73%	0.71%	1.02%	1.00%
Isolation/Impact Parameter	2.99%	0.73%	2.12%	0.11%
Total	20.04%	5.29%	13.11%	1.02%

The lepton trigger uncertainty dominates in the 4μ channel, while the dominant sources of uncertainty for the $4e$, $2e2\mu$, and $2\mu 2e$ channels are electron reconstruction and identification. There are two main reasons for this. The first is that electron reconstruction and ID are more susceptible to pileup than muon identification (since pileup/underlying event primarily create extraneous ID/calorimeter deposits rather than MS tracks). As discussed in Section 4.2, the increase in pileup between 2011 and 2012 means that 2012 electron uncertainties are expected to be higher. The second reason is that the scale factors used to compute the electron identification uncertainty are derived from the predecessor of likelihoodID, which is the electron identification algorithm used in this thesis. Scale factors from this previous algorithm (multileptonID) are used because the updated values for likelihoodID had yet to become available at the time of writing. However, given that the working point used for likelihoodID was specifically designed as a replacement for multileptonID (tuned to have identical signal efficiency with improved background rejection), these uncertainties are an appropriate, and likely conservative, estimate of the uncertainty on electron identification. A reduction in this uncertainty is expected when the scale factors for likelihoodID are released and implemented, due to the improvement in background rejection compared to multileptonID.

6.4. Fiducial Cross-section for $\mathbf{Z} \rightarrow \ell^+\ell^-\ell^+\ell^-$

The overall strategy for extracting the $Z \rightarrow \ell^+\ell^-\ell^+\ell^-$cross-section consists of two parts. First, the four-lepton cross-section is measured in a fiducial volume that reflects the acceptance of the detector and the requirements imposed by the event selection. These measurements are then extrapolated from the fiducial region to the phase space region defined in Equation 1.1.

Measuring a fiducial cross-section can itself be divided into two steps, separating theoretical losses in efficiency from experimental losses. These two types of inefficiency are distinguished by defining a fiducial volume which targets events within the phase space with similar generator-level features to those targeted with the (reconstruction-level) analysis selection.

The fiducial selection must be applied at generator-level, and therefore should be able to be evaluated using only particle four-vectors produced by MC generators. The kinematic, dilepton mass, J/ψ veto, and object separation cuts are easily translated from the analysis cuts shown in Table 5.3 into generator-level requirements for a fiducial volume. On the other hand, track and calorimeter isolation cuts cannot be applied in the fiducial selection, as they depend on the results of electromagnetic and hadronic showering, as well as on pileup conditions and the underlying event, both of which are added after the generation of the hard scatter. The impact parameter cuts cannot be applied at generator level either, since the origin of all generator-level four-vectors is considered to be the primary vertex. All three of these requirements omitted from the description of the fiducial volume are therefore regarded as experimental inefficiencies. A summary of the fiducial volume is given in Table 6.6.

Table 6.6.: Summary of the fiducial volume definition. All quantities are taken from generator-level 4-vectors.

$p_T(\ell 1) > 20$ GeV
$p_T(\ell 2) > 15$ GeV
$p_T(\ell 3) > 10$ GeV (if electron), > 8 GeV (if muon)
$p_T(\ell 4) > 7$ GeV(if electron), > 4 GeV (if muon)
$\|\eta\| < 2.7$ for all muons
$\|\eta\| < 2.5$ for all electrons
$\Delta R(\ell, \ell') > 0.1$ if ℓ, ℓ' have same flavour; > 0.2 if opposite flavour
$M_{\ell^+\ell^-} > 20$ GeV for at least one SFOS pair
$M_{\ell^+\ell^-} > 5$ GeV for all SFOS pairs
$80 < M_{4\ell} < 100$ GeV (implicit from phase space requirement)

The theoretical efficiency for fiducial volume acceptance, $A_{4\ell}$, can be defined as

$$A_{4\ell} = \frac{\text{\# of events passing Fiducial Selection}}{\text{\# of events in Phase Space}}. \tag{6.1}$$

The experimental efficiency, $C_{4\ell}$ is defined as

$$C_{4\ell} = \frac{\text{\# of events passing Analysis Selection}}{\text{\# of events passing Fiducial Selection}}, \tag{6.2}$$

and includes the trigger, reconstruction, and object identification efficiency corrections described in Section 6.3.

Using these definitions, both fiducial and analysis selections are applied to the POWHEG signal MC sample, using the event's truth-level 4-vectors to require them to fall within the phase space and fiducial volume, and then using reconstruction-level data to apply the analysis selection to those events passing the fiducial selection. The product of the theoretical and experimental efficiencies, $\varepsilon_{4\ell} = A_{4\ell} \times C_{4\ell}$, is interpreted as the overall efficiency for experimentally observing events generated in the defined phase space. A summary of these efficiencies is presented in Table 6.7.

Table 6.7.: A summary of theoretical, experimental, and overall efficiencies for the POWHEG signal samples.

	$A_{4\ell}$	$C_{4\ell}$	$\varepsilon_{4\ell} = A_{4\ell} \times C_{4\ell}$
$4e$	5.51 %	33.77 %	1.86 %
$2e2\mu$	11.10 %	51.63 %	5.73 %
$2\mu 2e$	6.09 %	41.69 %	2.54 %
4μ	13.37 %	65.50 %	8.76 %

The fiducial cross-section can be defined in terms of $C_{4\ell}$ by the following formula

$$\sigma_{\text{fid}}(\text{Z} \to \ell^+\ell^-\ell^+\ell^-) = \frac{N_{\text{obs}} - N_{\text{BG}}}{\mathcal{L} \cdot C_{4\ell}}, \tag{6.3}$$

where N_{obs} is the number of selected data events, N_{BG} is the total MC background estimate (given in Table 6.2), and $\mathcal{L}$ is the integrated luminosity for the 2012 dataset, 20.3 fb^{-1}.

Ignoring uncertainties on the background estimate, σ_{fid} is affected by uncertainties in three factors. Statistical uncertainties come from the Poisson statistics governing N_{obs}. Systematic uncertainties enter as experimental uncertainties on $C_{4\ell}$, as discussed in Section 6.3. Also discussed in that section was the luminosity uncertainty, which gives a $\pm 2.8\%$ uncertainty on $\mathcal{L}$. In Table 6.8, fiducial cross-section measurements along with their three independent uncertainty components are presented.

In the next section, the fiducial region measurements are extrapolated to the overall phase space (80 GeV $< M_{4\ell} <$ 100 GeV; $M_{\ell^+\ell^-} >$ 4 GeV), and a combination of the four analysis channels is used to compute a measurement of the $\text{Z} \to \ell^+\ell^-\ell^+\ell^-$ branching ratio.

Table 6.8.: Measurements of the fiducial $\mathrm{Z} \to \ell^+\ell^-\ell^+\ell^-$ cross-section for all four channels, with corresponding uncertainties.

	N_{obs}	N_{BG}	$C_{4\ell}$	σ_{fid} (fb)
$4e$	16	0.13	33.77%	2.3 ± 0.6 (stat.) $\pm\, 0.5$ (syst.) $\pm\, 0.1$ (lumi.)
$2e2\mu$	47	0.38	51.63%	4.5 ± 0.7 (stat.) $\pm\, 0.2$ (syst.) $\pm\, 0.1$ (lumi.)
$2\mu 2e$	15	0.42	41.69%	1.7 ± 0.5 (stat.) $\pm\, 0.2$ (syst.) $\pm\, 0.1$ (lumi.)
4μ	69	0.46	65.50%	5.2 ± 0.6 (stat.) $\pm\, 0.1$ (syst.) $\pm\, 0.1$ (lumi.)

6.5. Phase Space Cross-section and $\mathrm{Z} \to \ell^+\ell^-\ell^+\ell^-$ Branching Ratio

The phase space for this analysis has been defined in Equation 1.1, and values of $A_{4\ell}$ and $C_{4\ell}$ for the POWHEG signal MC samples have been given in Table 6.7. The phase space cross-section is defined both absolutely and as an extrapolation from the fiducial measurements as

$$\sigma_{\mathrm{PS}}(\mathrm{Z} \to \ell^+\ell^-\ell^+\ell^-) = \frac{N_{\mathrm{obs}} - N_{\mathrm{BG}}}{\mathcal{L} \cdot \varepsilon_{4\ell}} = \frac{N_{\mathrm{obs}} - N_{\mathrm{BG}}}{\mathcal{L} \cdot C_{4\ell} \cdot A_{4\ell}} = \frac{\sigma_{\mathrm{fid}}}{A_{4\ell}}. \tag{6.4}$$

In Table 6.9, measurements of the $\mathrm{Z} \to \ell^+\ell^-\ell^+\ell^-$ phase space cross-section are compared to theoretical predictions obtained from direct computations using the POWHEG event generator. The measured cross-sections are consistent within uncertainties with the SM predictions for all four channels.

Table 6.9.: Comparison of measurements of the total $\mathrm{Z} \to \ell^+\ell^-\ell^+\ell^-$ cross-section in the phase space compared with NLO theory predictions from POWHEG.

	$A_{4\ell}$	Theoretical σ_{PS} (fb)	Measured σ_{PS} (fb)
$4e$	5.51%	36.5 ± 0.1	42 ± 11 (stat.) $\pm\, 8$ (syst.) $\pm\, 1$ (lumi.)
$2e2\mu$	11.10%	34.7 ± 0.1	40 ± 6 (stat.) $\pm\, 2$ (syst.) $\pm\, 1$ (lumi.)
$2\mu 2e$	6.09%	34.8 ± 0.1	28 ± 7 (stat.) $\pm\, 4$ (syst.) $\pm\, 1$ (lumi.)
4μ	13.37%	36.1 ± 0.2	39 ± 5 (stat.) $\pm\, 0.4$ (syst.) $\pm\, 1$ (lumi.)

The measured cross-sections in the four separate channels are now combined, first into same- and mixed-flavour cross-sections, and finally as an inclusive measurement

Table 6.10.: Combined phase space cross-section measurements (in fb) obtained by direct summation.

	$4e + 4\mu$	$2e2\mu + 2\mu 2e$
Combined	$81 \pm 12 \pm 9 \pm 2$ fb	$68 \pm 9 \pm 6 \pm 2$ fb
SM expected	72.6 ± 0.3 fb	69.5 ± 0.2 fb
	All four channels	
Combined	149 ± 15 (stat.) ± 15 (syst.) ± 4 (lumi.) fb	
Total expected	142.2 ± 0.4 fb	

of the $\mathrm{Z} \to \ell^+\ell^-\ell^+\ell^-$ process (for $\ell = e, \mu$). For simplicity, this is done with a direct summation—adding statistical errors in quadrature, since they are uncorrelated between channels, adding luminosity errors arithmetically (since they are fully correlated between channels), and adding systematic errors arithmetically as well, being conservative in assuming 100% correlation between channels.

Adding electron and muon channels together requires the assumption of lepton universality, the principle that the couplings between leptons and gauge bosons (in this case the Z) are independent of lepton flavour. The same-flavour and mixed-flavour channels are added together first, however, given that the same-flavour channels are subjected to the lepton exchange interference terms discussed in Chapter 2. The results of these first two summations and the final combination are reported in Table 6.10.

The combined phase space cross-section is measured in agreement with the SM prediction. This cross-section is now used to measure the $\mathrm{Z} \to \ell^+\ell^-\ell^+\ell^-$ branching ratio. Because the four-lepton cross-section measurement is limited to a particular phase space (80 GeV $< M_{4\ell} <$ 100 GeV; $M_{\ell^+\ell^-} >$ 4 GeV), the result of this calculation will not be an inclusive branching ratio for the $\mathrm{Z} \to \ell^+\ell^-\ell^+\ell^-$ process. Instead, a phase-space-limited branching ratio is calculated using the following equation:

$$\mathrm{BR}(\mathrm{Z} \to \ell^+\ell^-\ell^+\ell^-) = \frac{\sigma_{\mathrm{PS}}(4e + 4\mu)(1 - f_t^{SF}) + \sigma_{\mathrm{PS}}(2e2\mu + 2\mu 2e)(1 - f_t^{OF})}{\sigma(\mathrm{pp} \to \mathrm{Z})} \tag{6.5}$$

where $\sigma(\mathrm{pp} \to \mathrm{Z})$ is the inclusive SM cross-section for Z production in pp collisions at $\sqrt{s} = 8$ TeV given in Table 2.1, and f_t is the t-channel (non-resonant) contribution to four-lepton production within the phase space ($f_t^{SF} = 4\%$ and $f_t^{OF} = 4.5\%$; see discussion in Chapter 2).

Determining whether a given event was produced via the resonant s-channel or non-resonant t-channel, is impossible. However, subtracting the expected t-channel contribution from the branching ratio calculation is reasonable, motivated by the Feynman diagrams shown in Figure 2.1. The s-channel diagram topologically represents a single Z boson decaying to four leptons, while the t-channel diagram represents the associated production of two Z bosons each following the usual $Z \to \ell^+\ell^-$ decay chain.

A theoretically-predicted value for the inclusive Z cross-section is used rather than a measured value since ATLAS results for inclusive Z production at $\sqrt{s} = 8$ TeV had not yet become available at the time of writing. Using a measured value would improve these results in that it would allow the cancellation of experimental systematic uncertainties common to both $Z \to \ell^+\ell^-\ell^+\ell^-$ and inclusive Z analyses. Such an analysis, using a measurement of the inclusive Z cross-section derived from a sample of ATLAS $Z \to \mu^-\mu^+$ and $Z \to e^-e^+$ events, would be a fruitful line of future inquiry, but is beyond the scope of this thesis.

Using Equation 6.5 and the combined phase space cross-section measurements from Table 6.10, the branching ratio of the Z boson to four leptons in the phase space defined by 80 GeV $< M_{4\ell} <$ 100 GeV and $M_{\ell^+\ell^-} > 4$ GeV is measured as:

$$\mathrm{BR}(Z \to \ell^+\ell^-\ell^+\ell^-) = (4.6 \pm 0.6) \times 10^{-6}. \tag{6.6}$$

This measurement agrees with the SM prediction of $(4.50 \pm 0.03) \times 10^{-6}$. It is also in agreement with the measurement made by CMS with $\sqrt{s} = 7$ TeV data, $BR(Z \to \ell^+\ell^-\ell^+\ell^-) = (4.2^{+0.9}_{-0.8}\ \text{(stat.)} \pm 0.2\ \text{(syst.)}) \times 10^{-6}$ [8].

Chapter 7.

Extension of the Phase Space to $M_{34} \geq 1$ GeV

7.1. Motivation

Given the observation of such low background in the signal region, it is natural to explore how the analysis selection might be loosened, to gain in signal acceptance without admitting significant amounts of new background contributions. Since the motivation for many event selection requirements was to follow the $\mathrm{H} \rightarrow \mathrm{ZZ}^{(*)} \rightarrow \ell^+\ell^-\ell^+\ell^-$ analysis, it is possible that some might be further relaxed for a measurement of the $\mathrm{Z} \rightarrow \ell^+\ell^-\ell^+\ell^-$ resonance.

Within the event selection in Table 5.3 that was used to obtain the results of the previous section, the kinematic requirements on the four leptons are already very close to the performance limits of the detector and trigger system. The p_T requirement on the two leading leptons must be kept high to maintain high trigger efficiency. Relaxing the requirements on the third leading lepton down to the object selection threshold (as for the fourth leading lepton) was considered, but resulted in only marginal gains in acceptance.

The ID and calorimeter isolation requirements are critical to the suppression of backgrounds from non-prompt leptons (see Table 6.2), and are therefore left fixed. The impact parameter requirements are important for suppressing cosmic rays in addition to non-prompt lepton backgrounds, and so are left unchanged as well.

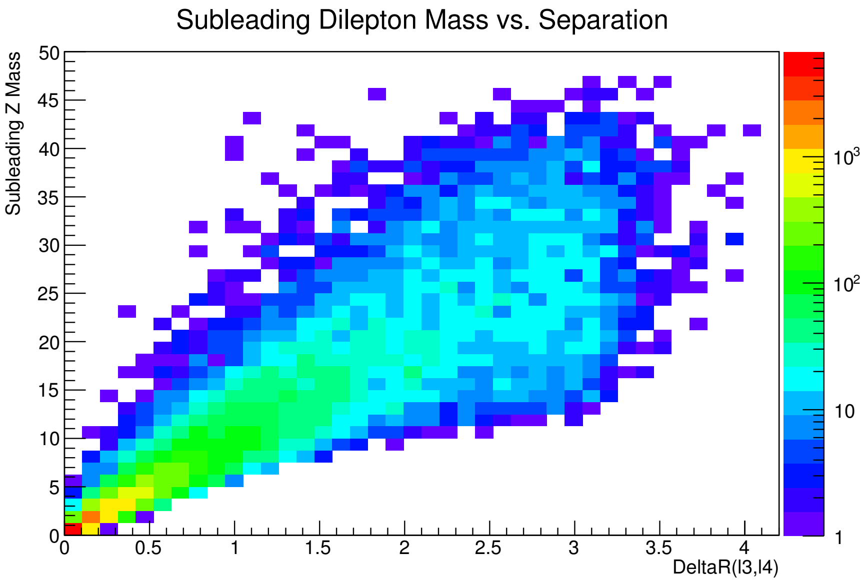

Figure 7.1.: A log-scale two-dimensional histogram illustrating the correlation between $M_{\ell\ell'}$ and $\Delta R(\ell, \ell')$, plotted at generator level.

This leaves only the dilepton mass cuts, object separation requirement, and J/ψ veto as possible candidates for relaxation. Figure 6.2 indicates that there is little to be gained from loosening the M_{12} cut, as it already has nearly 100% signal efficiency.

Loosening the M_{34} requirement is attractive because of the possibility of making a cross-section measurement in a more inclusive phase space. Such a change would necessitate loosening the J/ψ veto as well, since it places a minimum mass on all SFOS dilepton pairings (which includes M_{34}). In this case, a window-based J/ψ veto can be applied, which excludes events containing an SFOS dilepton pairing whose mass falls in the ranges defined below:

$$2.5\text{ GeV} < M_{\mathrm{e^-e^+}} < 3.6\text{ GeV} \qquad 2.95\text{ GeV} < M_{\mu^-\mu^+} < 3.25\text{ GeV}. \tag{7.1}$$

In addition, since lepton separation and dilepton mass are correlated, as shown in Figure 7.1, loosening or removing the ΔR requirements for the leptons in the quadruplet might be necessary to increase acceptance for events with low M_{34}. The colormap used in plotting this distribution follows a logarithmic scale, since as the cross-section for Z $\to$ $\ell^+\ell^-\ell^+\ell^-$ increases rapidly as `mllmin` approaches zero, high statistics are concentrated in the low-mass, low-separation bins.

Table 7.1 explores how much acceptance is gained by loosening the M_{34} and J/ψ veto cuts and either retaining or removing the object separation requirements in the analysis selection. Indicated in the table are the number of data events passing each level of loosened requirements; studies on signal MC samples show a similar pattern. The use of data as a proxy for signal relies on the assumption that backgrounds remain small as the cuts are loosened, which will be validated later in this section.

Table 7.1.: Number of events within the Z mass window selected from the ATLAS 2012 dataset for varying M_{34} and J/ψ veto requirements. 'ΔR' and '$\not{\Delta R}$' columns indicate selections with or without object separation requirements, respectively.

		4e		2e2μ		2μ2e		4μ	
M_{34} cut	J/ψ veto	ΔR	$\not{\Delta R}$	ΔR	$\not{\Delta R}$	ΔR	$\not{\Delta R}$	ΔR	$\not{\Delta R}$
5 GeV	$M_{\ell^+\ell^-} > 5$ GeV	16	16	47	47	15	16	69	69
5 GeV	Window; $M_{\ell^+\ell^-} > 1$ GeV	17	17	47	47	15	16	91	94
4 GeV	Window; $M_{\ell^+\ell^-} > 1$ GeV	19	19	54	54	20	21	107	111
3 GeV	Window; $M_{\ell^+\ell^-} > 1$ GeV	21	21	66	66	20	21	120	125
2 GeV	Window; $M_{\ell^+\ell^-} > 1$ GeV	23	23	81	81	25	26	139	144
1 GeV	Window; $M_{\ell^+\ell^-} > 1$ GeV	24	24	106	109	29	31	165	178
0 GeV	Window	24	27	109	155	29	32	169	308

The switch from the $M_{\ell^+\ell^-} > 5$ GeV to the window-based J/ψ veto leads to significant gains in the 4μ channel and a slight gain in the $4e$ channel. No change is observed in the mixed flavour-channels, because since no other SFOS pairings other than the primary and secondary dileptons are possible, they are unaffected by the J/ψ veto. An increase in statistics for all four channels is observed as the M_{34} cut is relaxed from > 5 GeV to > 1 GeV.

Until the final row of Table 7.1, the difference between acceptances when enforcing or omitting object separation requirements are small. This shows that despite the correlation observed in Figure 7.1, most events lie within the range of acceptance for the object separation cuts, even down to an M_{34} cut of > 1 GeV. It is only in the range of 0 GeV $< M_{34} <$ 1 GeV that most events fail to satisfy such a requirement.

In the two channels whose secondary dilepton is a pair of muons ($2e2\mu$, 4μ), a modest increase in statistics is observed when loosening the M_{34} cut while retaining object separation cuts. Omitting the latter, a significant increase in statistics is observed. This shows that low mass dimuons, even in the absence of an explicit M_{34} cut, can cause an event to be rejected by an object separation requirement (making such a cut, in effect, an implicit dilepton mass cut).

Similarly, in the two channels with a secondary dielectron ($4e$, $2\mu 2e$), no difference is observed between the penultimate and final rows when the object separation requirements are retained. This is consistent with observations from the other two channels. However, when the object separation requirement is removed, unlike in the previous instance where large gains are recorded, a small gain is realised in each channel. This is because electron reconstruction, with its 0.075×0.125 sliding window, and lepton overlap removal requirements, imposes implicit cuts on electron separation, hindering the resolution of many electron pairs with $\Delta R(\mathrm{e}^-, \mathrm{e}^+) < 0.1$.

That the identification of electron pairs with low ΔR would be less efficient than for close-by muon pairs is reasonable, given that electron reconstruction relies on pairing ID tracks with calorimeter deposits, which tend to be more spread in (η, ϕ) due to the physics of electromagnetic showering. Muon reconstruction, on the other hand, relies on combining ID tracks with MS tracks, and since tracking detectors have higher resolution than calorimeters, more muon pairs with very low $\Delta R(\mu^-, \mu^+)$ (and therefore low $M_{\mu^-\mu^+}$) are able to be resolved during reconstruction.

Despite the sizeable increase in acceptance obtained in two of four channels when the M_{34} and ΔR requirements are completely removed, both must be retained at some level due to simulation and detector limitations. Without an explicit $M_{\ell^+\ell^-}$ cut on all SFOS pairs (including M_{34}) in each event, the production of MC samples is required to be fully inclusive and accurately account for the production of SFOS leptons down to the respective mass threshold for each flavour ($2 \times m_{\mathrm{e}^-} \approx 0.00102$ GeV, $2 \times m_{\mu^-} \approx 0.211$ GeV).

On the detector side, the performance of electron reconstruction dictates that electron separation requirements be retained. Removing separation requirements for muons might be possible, but would necessitate performance studies which are beyond the scope of this thesis. Lepton separation requirements are therefore retained in the event selection.

Table 7.2 highlights the proposed changes to the phase space, fiducial volume, and analysis selection. The analysis presented in Chapter 6 will be referred to as the 'high-mass' selection, and this new extended analysis as the 'low-mass' selection.

Table 7.2.: A summary of changes to the original phase space, fiducial volume, and analysis selection implemented to increase signal acceptance.

'High-mass' selection	'Low-mass' selection
Phase Space	
80 GeV $< M_{4\ell} <$ 100 GeV	80 GeV $< M_{4\ell} <$ 100 GeV
$M_{\ell^+\ell^-} >$ 4 GeV	$M_{\ell^+\ell^-} >$ 1 GeV
Fiducial Volume	
Kinematics	Kinematics
Object separation	Object separation
$M_{\ell^+\ell^-} >$ 5 GeV for all SFOS pairs	$M_{\ell^+\ell^-} >$ 1 GeV for all SFOS pairs
	J/ψ window veto as defined in Eq. 7.1
Analysis Selection (shared requirements omitted)	
$M_{34} >$ 5 GeV	$M_{34} >$ 1 GeV
$M_{\ell^+\ell^-} >$ 5 GeV for all SFOS pairs	$M_{\ell^+\ell^-} >$ 1 GeV for all SFOS pairs
	J/ψ window veto as defined in Eq. 7.1

7.2. Low-Mass POWHEG Samples: Validation and Issues

As described in Section 4.1, $Z^{(*)}Z^{(*)} \to \ell^+\ell^-\ell^+\ell^-$ samples were produced using POWHEG with `mllmin` = 4 GeV and used for the results presented in Chapter 6. 'Low-mass' POWHEG samples were also produced with `mllmin` = 0.25 GeV to analyse potential expansions of the phase explored in the preceding section.

To validate these 'low-mass' POWHEG MC samples, the 'high-mass' (`mllmin` = 4 GeV) samples and 'low-mass' (`mllmin` = 0.25 GeV) samples are subjected to the 'high-mass' selection (see Table 7.2). Since the high-mass analysis accepts a region of phase space that is common to both samples, they are expected to give consistent $A_{4\ell}$ and $C_{4\ell}$ values in this region. A comparison of the efficiencies for these two samples is given in Table 7.3.

Within MC statistical uncertainties, the efficiencies for both the low-mass and high-mass POWHEG signal samples are consistent within the common region of phase space

Table 7.3.: Comparisons of theoretical and experimental efficiencies from 'low-mass' and 'high-mass' POWHEG signal samples for the 'high-mass' analysis. Uncertainties are due to MC statistics.

Channel	`mllmin` (GeV)	$A_{4\ell}$ (%)	$C_{4\ell}$ (%)	$\varepsilon = A_{4\ell} \times C_{4\ell}$ (%)
$4e$	4	5.51 ± 0.03	33.8 ± 0.3	1.86 ± 0.02
	0.25	5.5 ± 0.1	33.5 ± 0.6	1.9 ± 0.1
$2e2\mu$	4	11.1 ± 0.1	51.6 ± 0.2	5.7 ± 0.1
	0.25	11.4 ± 0.4	50.9 ± 0.6	5.8 ± 0.2
$2\mu 2e$	4	6.1 ± 0.1	41.7 ± 0.3	2.54 ± 0.03
	0.25	5.6 ± 0.3	41.1 ± 0.8	2.31 ± 0.13
4μ	4	13.4 ± 0.2	65.5 ± 0.2	8.8 ± 0.1
	0.25	12.9 ± 0.3	64.1 ± 0.5	8.3 ± 0.3

defined by the high-mass analysis. This shows that POWHEG is modelling the shape of the Z $\rightarrow \ell^+\ell^-\ell^+\ell^-$ signal correctly for low values of `mllmin`. This is confirmed by plotting shape comparisons for several variables relevant to the analysis selection in Figures 7.2, 7.3, 7.4, and 7.5. These plots compare data, high- and low-mass POWHEG, and the Sherpa cross-check samples (which are inclusive down to threshold `mllmin`), with all three MC samples normalised to match the observed data. These plots allow comparisons of distribution shapes between:

1. The low-mass POWHEG sample to the high-mass sample.
2. Different generators (i.e. POWHEG vs. Sherpa).
3. Data and all three MC samples.

Agreement between the shape of the data and all three MC samples is observed within statistical uncertainties. The low- and high-mass POWHEG (and Sherpa) samples are also observed to exhibit shape agreement in the common validation region.

Despite this shape agreement, the three MC samples are found to diagree in overall normalisation within the signal region. This is illustrated in Figure 7.6, which shows the same distribution as that plotted in Figure 7.4, but with each MC normalised to its calculated cross-section. Their normalisations exhibit large disagreement, with low-mass POWHEG consistently low and Sherpa systematically high compared to the nominal (high-mass) POWHEG sample.

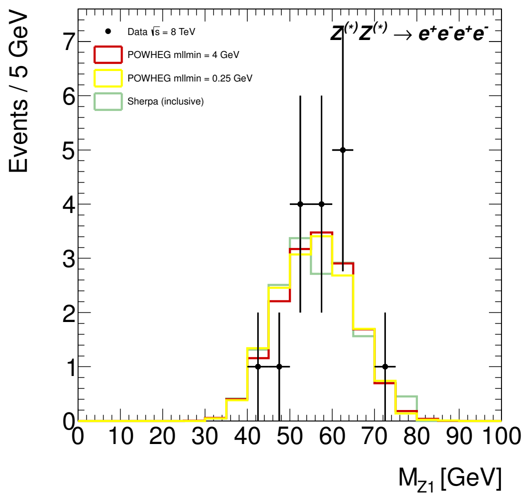

(a) $4e$ channel

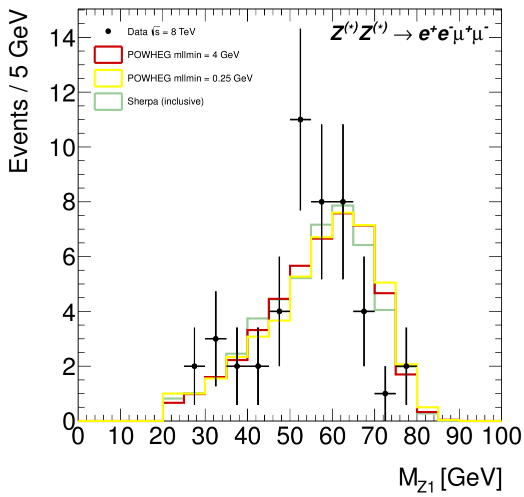

(b) $2e2\mu$ channel

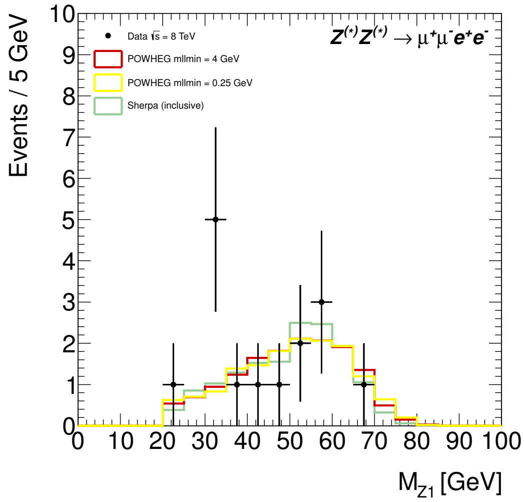

(c) $2\mu2e$ channel

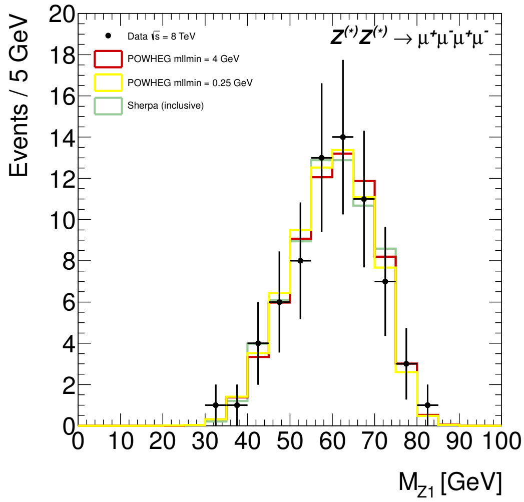

(d) 4μ channel

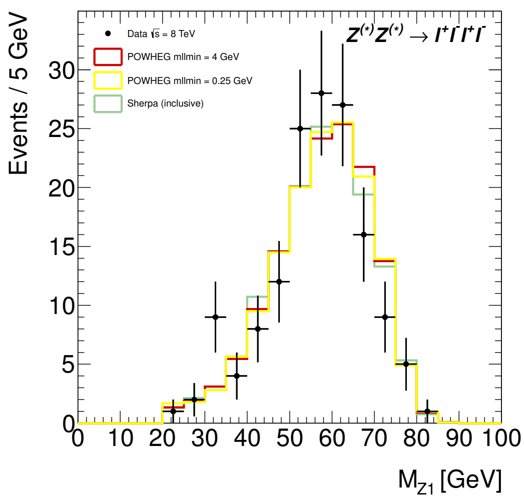

(e) Inclusive channel

Figure 7.2.: Shape comparisons of the mass of the primary dilepton (M_{12}) from the high-mass analysis, plotted for each individual channel, as well as the inclusive total of all four channels.

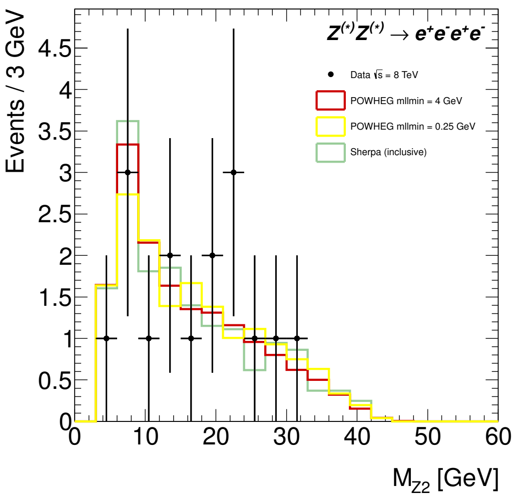

(a) $4e$ channel

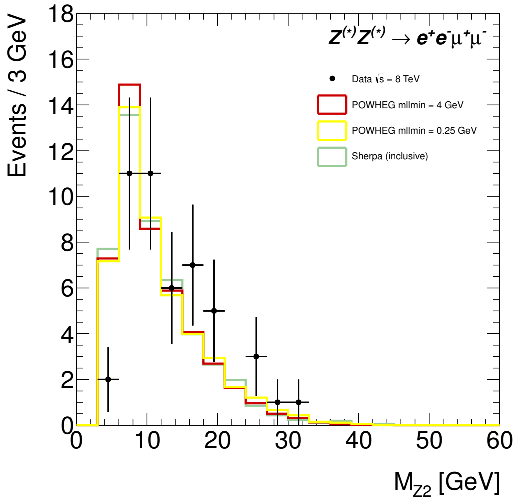

(b) $2e2\mu$ channel

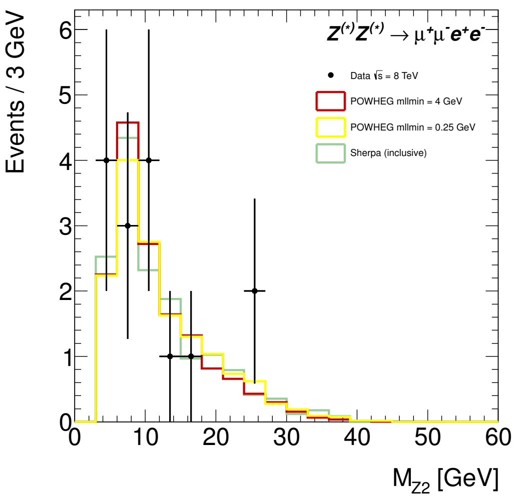

(c) $2\mu2e$ channel

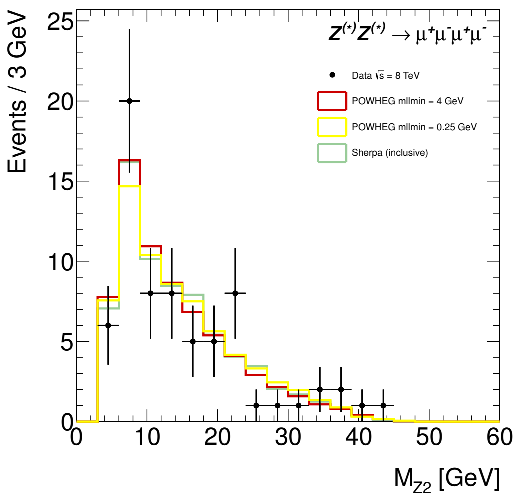

(d) 4μ channel

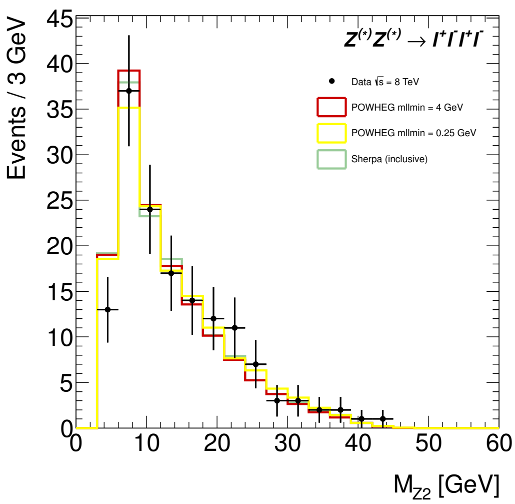

(e) Inclusive channel

Figure 7.3.: Shape comparisons of the mass of the secondary dilepton (M_{34}) from the high-mass analysis, plotted for each individual channel, as well as the inclusive channel.

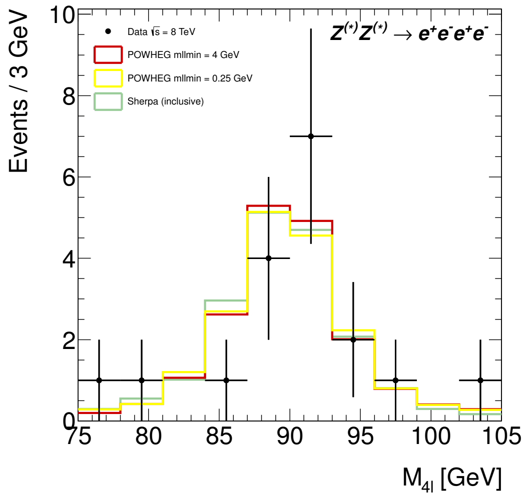

(a) $4e$ channel

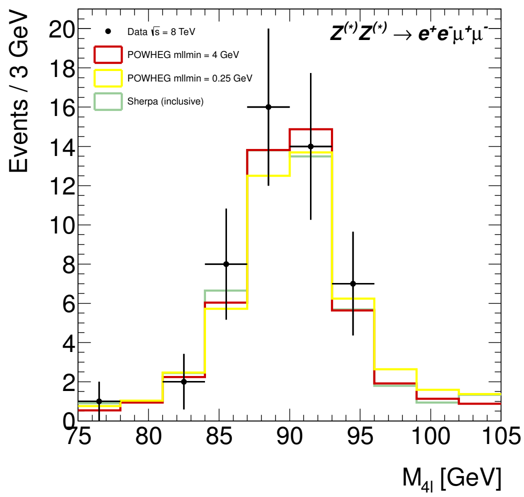

(b) $2e2\mu$ channel

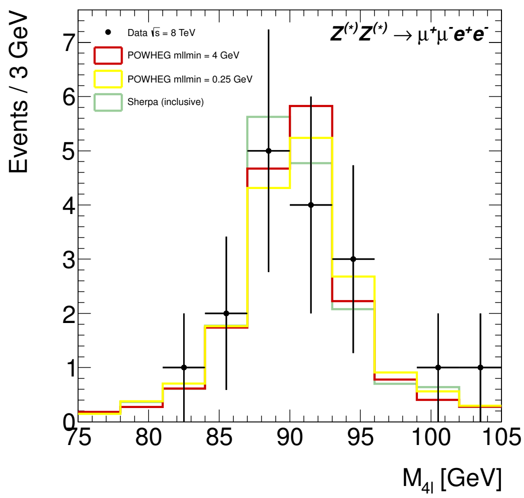

(c) $2\mu 2e$ channel

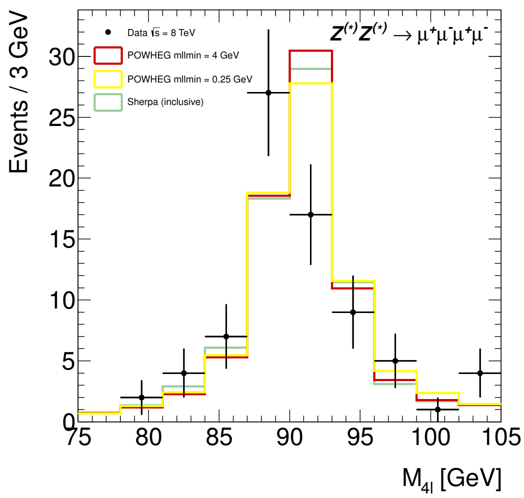

(d) 4μ channel

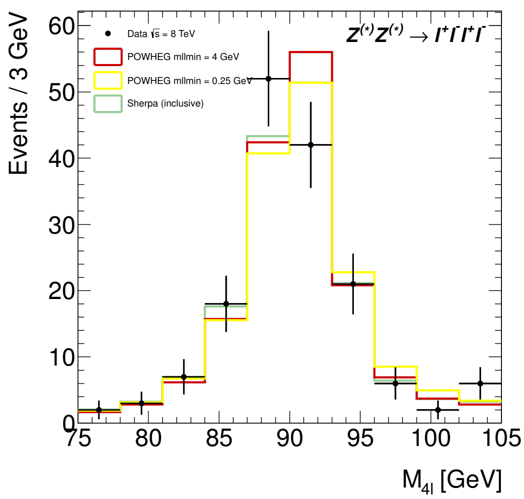

(e) Inclusive channel

Figure 7.4.: Shape comparisons of 4-lepton mass distributions from the high-mass analysis, plotted for each individual channel, as well as the inclusive channel.

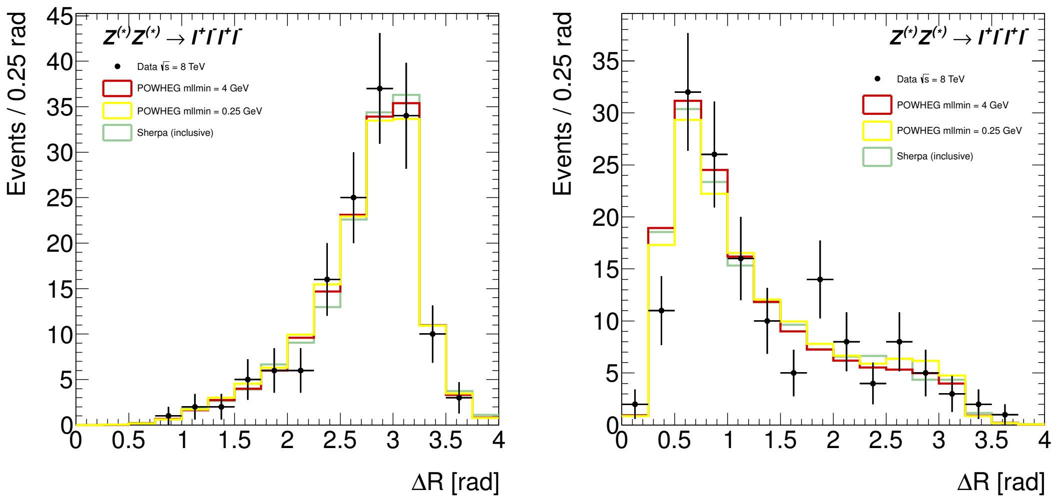

Figure 7.5.: Shape comparisons of the separation of the leptons comprising the (left) primary dilepton and (right) secondary dilepton from the high-mass analysis in the inclusive channel.

At the time of writing, these differences have yet to be understood. Small-scale studies have shown that the deviation from the normalisation of the `mllmin` = 4 GeV sample increases as `mllmin` is lowered. This means that for an analysis requiring $M_{\ell^+\ell^-} \geq 1$ GeV, a POWHEG sample with `mllmin` = 0.25 GeV is not ideal. A request for ATLAS production of new MC samples with `mllmin` = 1 GeV, to more closely reflect the extended phase space in this particular analysis, has been submitted, but these new samples did not become available in time for consideration in this thesis.

Several key variables are plotted to illustrate the changes introduced by the low-mass analysis. 'Low-mass' POWHEG MC samples are normalised to their anomalously small overall cross-section to illustrate the scale of the effect, but still allow for shape comparison between data and MC simulation. Figures 7.7 and 7.8 show the new M_{12} and M_{34} distributions, respectively. Figure 7.9 shows the four-lepton mass spectra for each channel of the 'low-mass' analysis. Finally, Figure 7.10 shows the separation between the leptons comprising the primary and secondary dileptons. Compared to the distributions shown in Figure 6.5, the 'low-mass' selection shows a marked increase in acceptance for events with low separation between the constituents of the secondary dilepton, as expected given its extension to low dilepton mass. These distributions indicate an overall excess of data over MC simulation, which is especially visible in the $2e2\mu$ and 4μ channels.

In Section 7.3, fiducial and phase space cross-sections derived from the low-mass analysis are presented, since these depend only on the $A_{4\ell}$ and $C_{4\ell}$ efficiencies which have

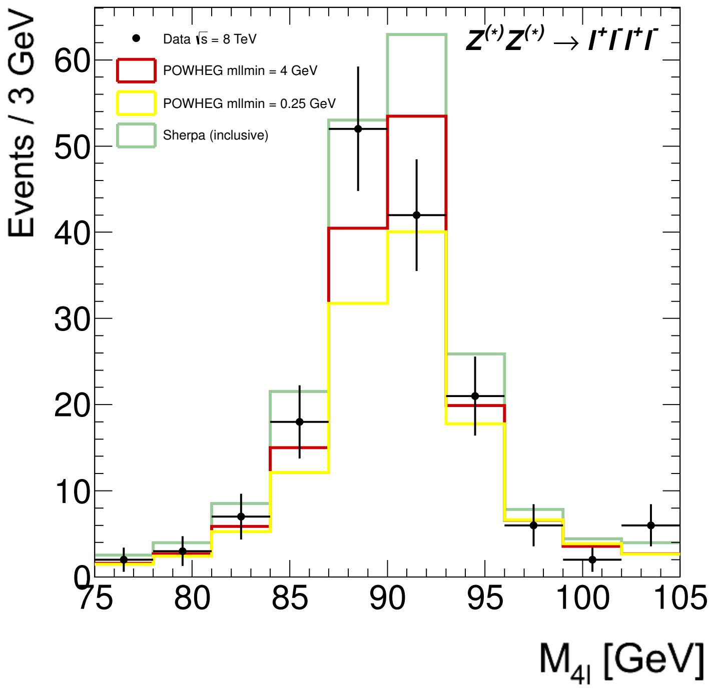

Figure 7.6.: Inclusive four-lepton mass distribution from the 'high-mass' selection, showing data compared to predictions from Sherpa, POWHEG with $mllmin = 4$ GeV and POWHEG with $mllmin = 0.25$ GeV, normalised to their respective predicted cross-sections. A significant normalisation disagreement among the three samples is observed.

been shown to be consistent between the low- and high-mass samples in the high-mass region.

7.3. Fiducial and Extended Phase Space Cross-sections

Having validated the $A_{4\ell}$ and $C_{4\ell}$ efficiencies from the low-mass POWHEG MC samples, fiducial and phase space cross-sections for the $\mathrm{Z} \to \ell^+\ell^-\ell^+\ell^-$ process can be measured in the extended phase space defined by 80 GeV $< M_{4\ell} <$ 100 GeV and $M_{\ell^+\ell^-} \geq 1$ GeV.

Table 7.4 shows the cutflow for the low-mass analysis applied to the full ATLAS 2012 dataset. In total, 324 $\mathrm{Z} \to \ell^+\ell^-\ell^+\ell^-$ candidates are selected, compared with the 147 identified by the event selection used in Chapter 6. Table 7.5 shows a summary of selected events from data, along with signal and background expectations estimated from MC samples. The signal prediction is systematically low due to the normalisation

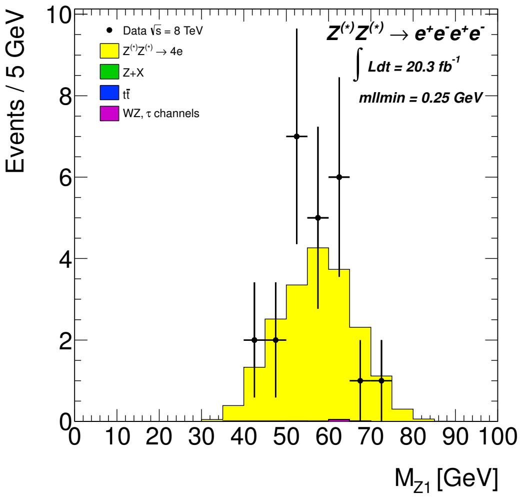

(a) $4e$ channel

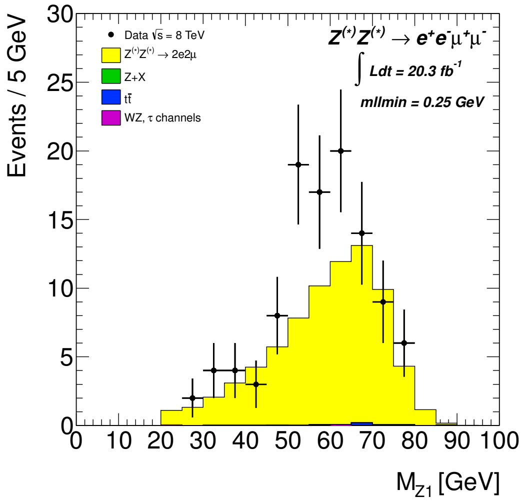

(b) $2e2\mu$ channel

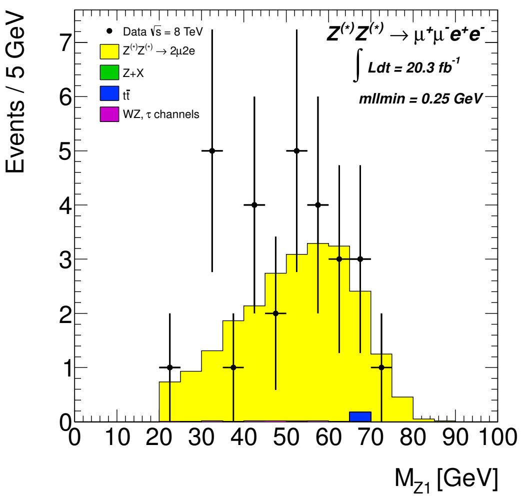

(c) $2\mu 2e$ channel

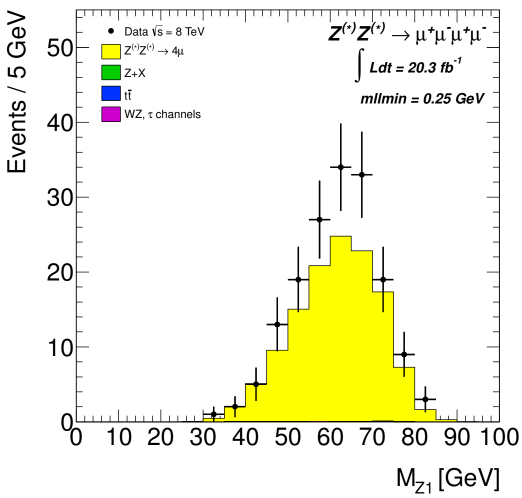

(d) 4μ channel

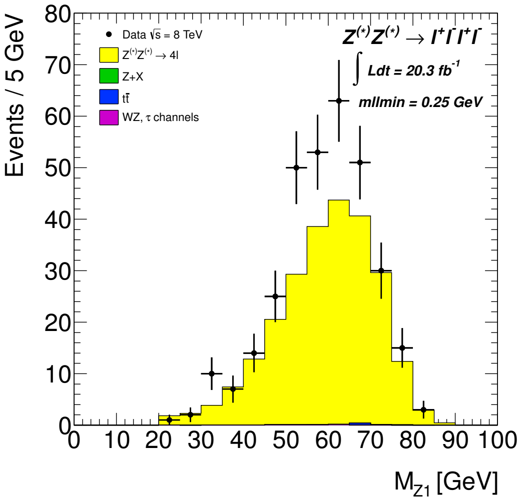

(e) Inclusive channel

Figure 7.7.: Distributions of the mass of the primary dilepton (M_{12}) from the low-mass analysis, plotted for each individual channel, as well as the inclusive total of all four channels.

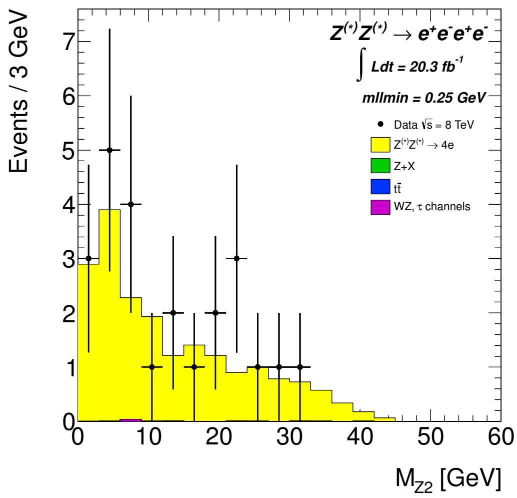

(a) 4e channel

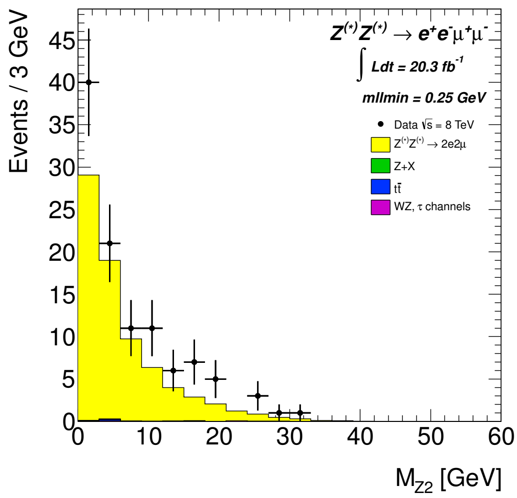

(b) 2e2μ channel

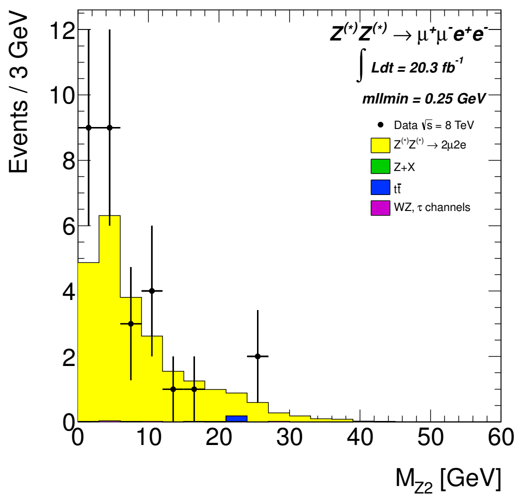

(c) 2μ2e channel

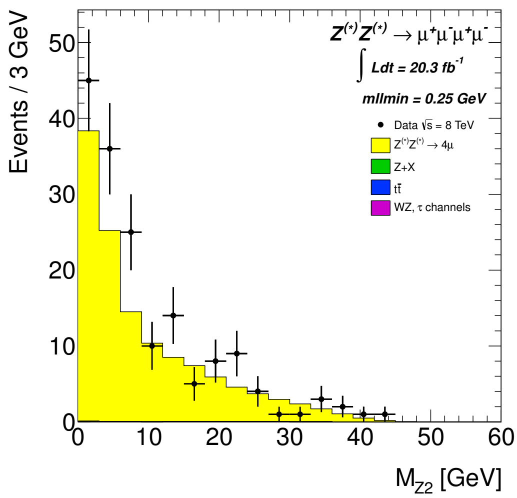

(d) 4μ channel

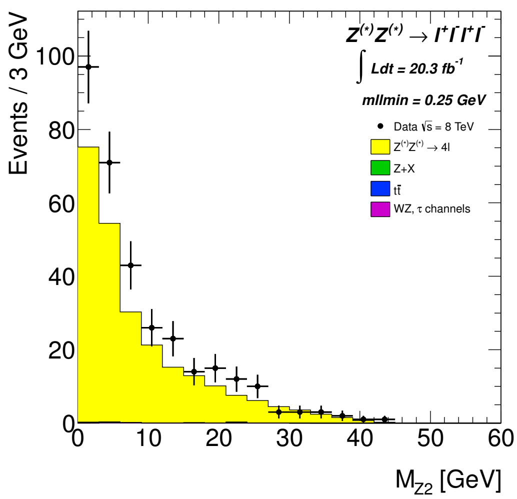

(e) Inclusive channel

Figure 7.8.: Distributions of the mass of the secondary dilepton (M_{34}) from the low-mass analysis, plotted for each individual channel, as well as the inclusive channel.

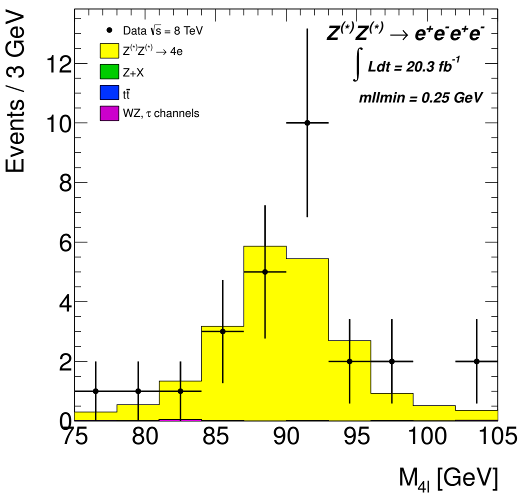

(a) 4e channel

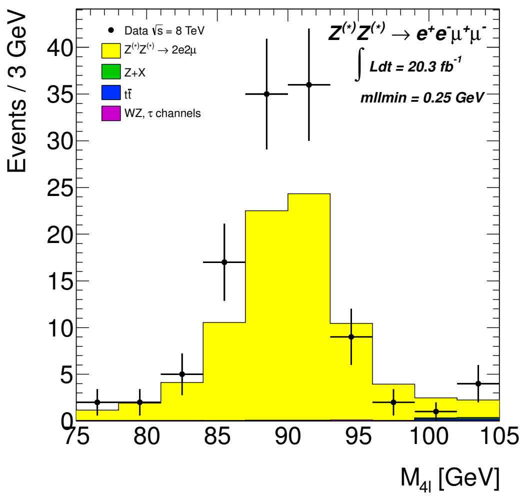

(b) 2e2μ channel

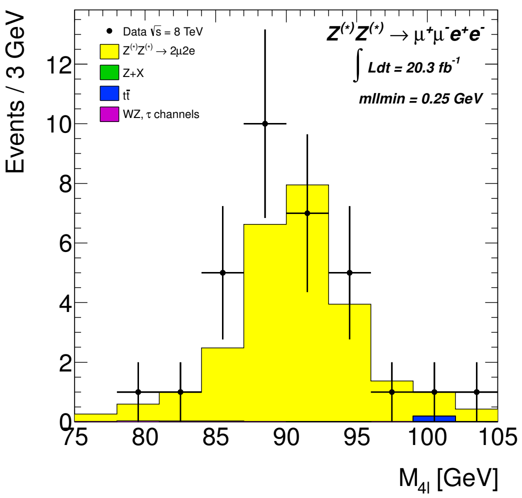

(c) 2μ2e channel

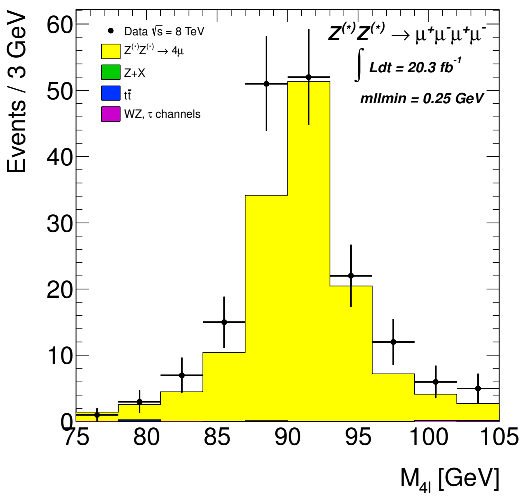

(d) 4μ channel

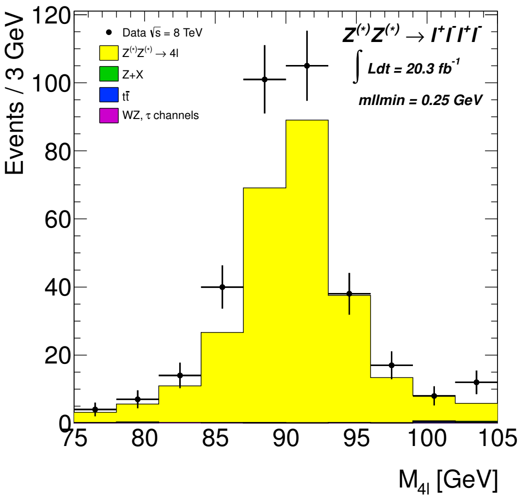

(e) Inclusive channel

Figure 7.9.: Four-lepton mass distributions from the low-mass analysis, plotted for each individual channel, as well as the inclusive channel.

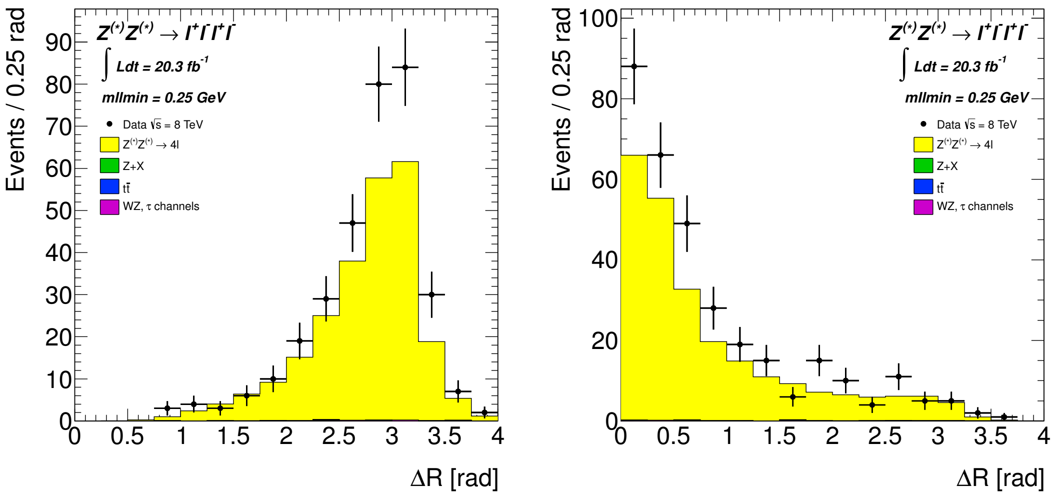

Figure 7.10.: Plots of the separation of the leptons comprising the (left) primary dilepton and (right) secondary dilepton from the low-mass analysis, plotted for the inclusive channel.

issue discussed in the previous section. The background expectation is estimated from MC simulations, using new `mllmin` = 0.25 GeV samples produced with POWHEG to estimate the background contribution of decay channels of the $Z^{(*)}Z^{(*)}$ process involving $\tau^{\pm}$ leptons. These estimates indicate that background acceptance remains low for the extended analysis. This is further supported by the observation of low-population sidebands observed in all channels for the four-lepton mass resonances plotted in Figure 7.9.

Fiducial cross-sections in the extended phase space (80 GeV $< M_{4\ell} <$ 100 GeV; $M_{\ell^+\ell^-} >$ 1 GeV) are measured for the extended fiducial volume described in Table 7.2 using Equation 6.3. Systematic uncertainties are assessed using the methods described in Section 6.3, and the results are displayed in Table 7.6.

Equation 6.4 is used to extrapolate the measurements of σ_{fid} into the extended phase space. The results are shown in Table 7.7. Measurements in the $4e$ and $2\mu 2e$ channels are consistent with theory, however, in the 4μ and $2e2\mu$ channels, the data significantly exceed the theory prediction. This is due to the MC cross-section normalisation issue discussed earlier.

Table 7.4.: Low-mass analysis cutflow for the full ATLAS 2012 dataset. In total, 347 $Z \rightarrow \ell^+\ell^-\ell^+\ell^-$ candidates are selected.

	$4e$	$2e2\mu$	$2\mu 2e$	4μ
4 SFOS leptons	423	7650	3001	46629
Kinematics	284	3137	1128	12137
Trigger Matched	283	3111	1117	11696
M_{12}	282	2736	902	10853
M_{34}	276	2193	898	9403
Object Separation	273	1744	701	5155
J/ψ veto	226	1620	615	3988
Track Isolation	145	435	192	596
Calo Isolation	117	355	161	478
Impact Parameter	114	296	153	413
Z Mass Window	24	106	29	165

Table 7.5.: Summary of expected and observed events for the low-mass analysis selection.

Channel	Data	Signal	N_{BG}^{tot}
$4e$	24	19.49	0.097
$2e2\mu$	106	74.38	0.804
$2\mu 2e$	29	23.48	0.347
4μ	165	126.89	0.459

Table 7.6.: Fiducial cross-sections for the four channels in the low-mass fiducial volume defined in Table 7.2.

Channel	$C_{4\ell}$	Measured σ_{fid} (fb)
$4e$	$(34.0 \pm 0.6)\%$	3.5 ± 0.7 (stat.) $\pm\, 0.7$ (syst.) $\pm\, 0.1$ (lumi.)
$2e2\mu$	$(52.0 \pm 0.5)\%$	10.0 ± 1.0 (stat.) $\pm\, 0.5$ (syst.) $\pm\, 0.3$ (lumi.)
$2\mu 2e$	$(41.8 \pm 0.7)\%$	3.4 ± 0.6 (stat.) $\pm\, 0.5$ (syst.) $\pm\, 0.1$ (lumi.)
4μ	$(64.5 \pm 0.4)\%$	12.6 ± 1.0 (stat.) $\pm\, 0.13$ (syst.) $\pm\, 0.4$ (lumi.)

These fiducial and total phase-space cross-sections are presented as preliminary measurements, given that the mismatch between the normalisations of data and low-mass POWHEG MC samples has yet to be understood. Without solving this problem, it is

Table 7.7.: Cross-sections for the four channels calculated in the phase space defined by 80 GeV $< M_{4\ell} <$ 100 GeV, $M_{\ell^+\ell^-} > 1$ GeV.

Channel	$A_{4\ell}$	Measured σ_{PS} (fb)	Theory (fb)
$4e$	$(2.6 \pm 0.1)\%$	133 ± 27 (stat.) ± 27 (syst.) ± 4 (lumi.)	129 ± 3
$2e2\mu$	$(6.5 \pm 0.1)\%$	153 ± 15 (stat.) ± 8 (syst.) ± 4 (lumi.)	127 ± 7
$2\mu 2e$	$(2.7 \pm 0.1)\%$	124 ± 23 (stat.) ± 17 (syst.) ± 4 (lumi.)	127 ± 7
4μ	$(8.1 \pm 0.1)\%$	155 ± 12 (stat.) ± 2 (syst.) ± 4 (lumi.)	129 ± 3

difficult to obtain a theory estimate to which to compare the measured cross-sections. However, awaiting an improved understanding of Z $\rightarrow \ell^+\ell^-\ell^+\ell^-$ simulation at low `mllmin`, these measured cross-sections can be taken as preliminary experimental observations of σ_{fid} and σ_{PS} for the Z $\rightarrow \ell^+\ell^-\ell^+\ell^-$ process in the 80 GeV $< M_{4\ell} <$ 100 GeV, $M_{\ell^+\ell^-} > 1$ GeV phase space.

Chapter 8.

Analytical Fits to the Peak of the $Z \to \ell^+\ell^-\ell^+\ell^-$ Resonance

8.1. Motivation and Theory

The $Z \to \ell^+\ell^-\ell^+\ell^-$ peak provides a practical way to assess detector response to a known four-lepton resonance in order to cross-check measurements made in the similar $H \to ZZ^{(*)} \to \ell^+\ell^-\ell^+\ell^-$ regime. In this section, data and MC events selected by the extended phase space analysis presented in Chapter 7 are fitted with analytical PDFs to characterise the position of their peaks and their widths, in order to verify the accuracy of the four-lepton mass scale around $M_{4\ell} \approx M_Z$.

The four-lepton mass spectrum of resulting from the decay of an unstable particle of mass M and width Γ to a four-lepton final state can be modelled by a Breit-Wigner distribution, whose shape [51] is governed by

$$\sigma(M_{4\ell}) = BW(M, \Gamma) \propto \frac{\Gamma^2/4}{(M_{4\ell} - M)^2 + \Gamma^2/4}. \quad (8.1)$$

The spectra observed in the ATLAS detector represent the convolution of this underlying Breit-Wigner distribution with a Gaussian distribution, to model the resolution of the detector. Therefore, the following function is used to fit both data and MC spectra in order to evaluate the agreement of the four-lepton mass scale between them:

$$BW(M_{BW}, \Gamma_Z) \star Gaussian(\Delta M_G, \sigma), \tag{8.2}$$

where $\star$ represents analytical convolution, ΔM_G represents the mass bias due to Gaussian smearing, σ is a width proportional to the resolution of the detector, and Γ_Z is the total decay width of the Z boson, fixed to the PDG value of 2.49 GeV [52].

The RooFit toolkit [53] is used to perform unbinned maximum likelihood fits of the Z $\rightarrow \ell^+\ell^-\ell^+\ell^-$ peak as observed in both data and MC simulation. In this implementation, the Breit-Wigner mass M_{BW} and the Gaussian mass shift ΔM_G are combined into a single fitted mass parameter, which will be referred to as M.

Within the $Z^{(*)}Z^{(*)} \rightarrow \ell^+\ell^-\ell^+\ell^-$ spectrum, while the contributions of resonant s-channel diagrams can be modelled by the spectrum of a decaying particle, the non-resonant t-channel diagrams make a continuum contribution to the spectrum. This contribution is approximated in a second fitting strategy, by adding a uniform distribution with floating normalisation to the distribution described in Equation 8.2.

8.2. Results

Fits using the BW$\star$Gaussian functions omitting and including a floating offset are compared in Figures 8.1, 8.2, 8.3, and 8.4 in descending order of fit statistics (4μ, $2e2\mu$, $2\mu 2e$, $4e$). Improved visual agreement of the fits to both data and MC spectra is observed for the second fitting strategy, where a floating offset is allowed. The small visual disagreements that remain are likely due to the t-channel contribution not being uniform in the range of 80 GeV $< M_{4\ell} <$ 100 GeV (see Figure 2.2).

A summary of fitted parameters obtained using the function defined in Equation 8.2 is presented in Table 8.1. The locations of the mass peaks in data and MC spectra agree to within $\pm 1.5\sigma$ of the fitting uncertainties, and the resolution values also agree to within $\pm 1.7\sigma$. However, in the low-statistics channels ($4e$ and $2\mu 2e$), the widths of the spectra are not well-constrained by the data (see Figures 8.3 and 8.4).

Parameters obtained from the same function, but with a floating offset term, are included in Table 8.2 to show the parameters resulting from allowing the offset to float. Despite the visual improvements in fits using this strategy, agreement between data and MC parameters remains comparable. The mass parameters agree to within $\pm 2.0\sigma$, while the resolutions agree to within $\pm 1.6\sigma$ for the floating offset model. In the two lower-statistics channels, the resolution is again not highly constrained by the data.

These fits verify the accuracy of the four-lepton mass scale in the region of $M_{4\ell} \approx M_Z$ to within $\pm 1\%$. For both fitting strategies, the difference between data and MC mass scales is consistent with zero in the 4μ channel, which has the largest statistics and is therefore the most important to resonance mass measurements. Other channels have lower statistics, but all show better than 2σ agreement between data and MC parameters and confirm the accuracy of the mass scale to a precision of $\leq 1\%$. While this does not constitute a direct validation of the four-lepton mass scale for the newly discovered Higgs resonance at $M_{4\ell} \approx 125$ GeV, it does cross-check the accuracy of the scale in a similar four-lepton resonance with comparable invariant mass.

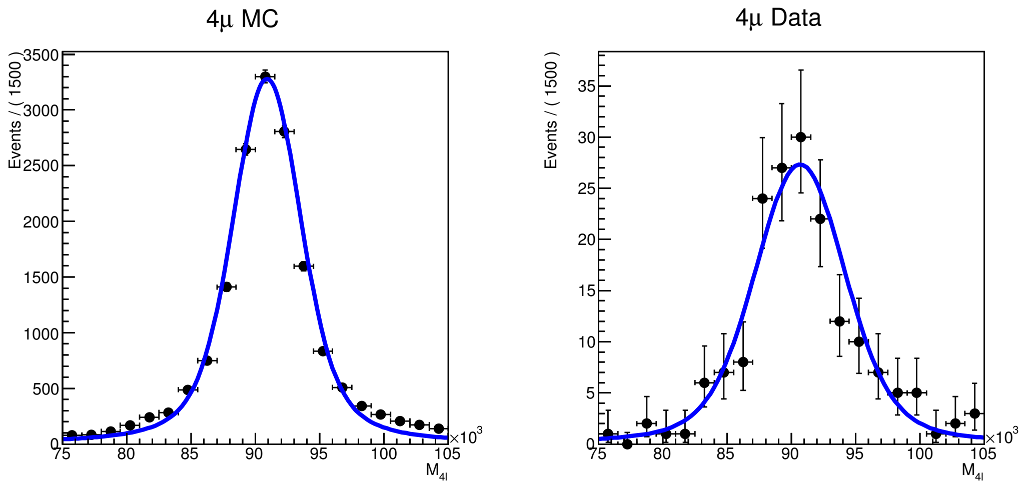

(a) Fits of the function defined in Eqn. 8.2 to MC signal (left) and data (right).

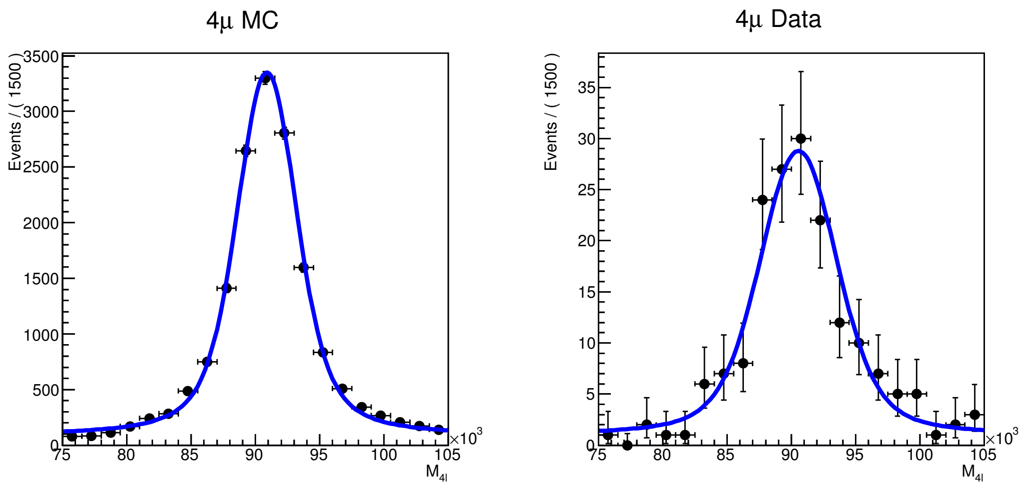

(b) Fits of the function defined in Eqn 8.2 to MC signal (left) and data (right), including a floating constant term.

Figure 8.1.: Results of the two mass fit strategies shown for the 4μ channel.

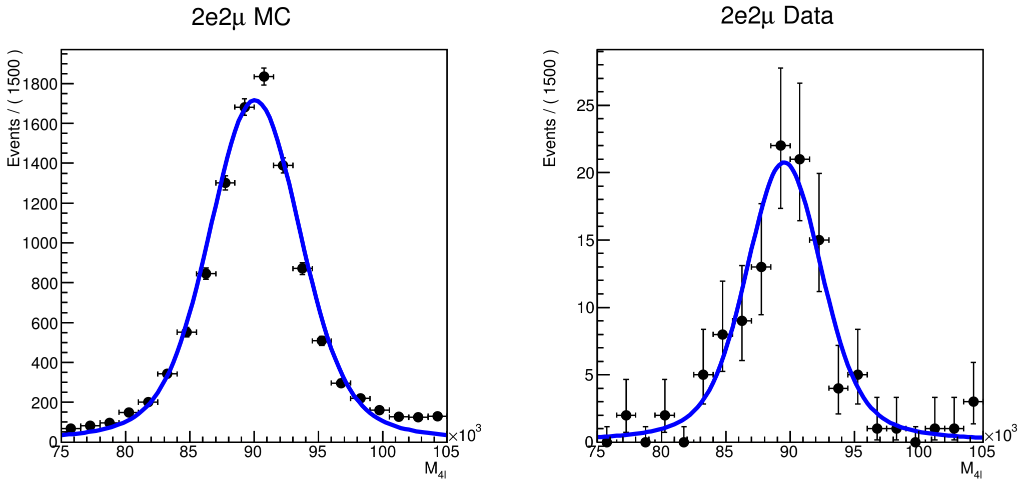

(a) Fits of the function defined in Eqn. 8.2 to MC signal (left) and data (right).

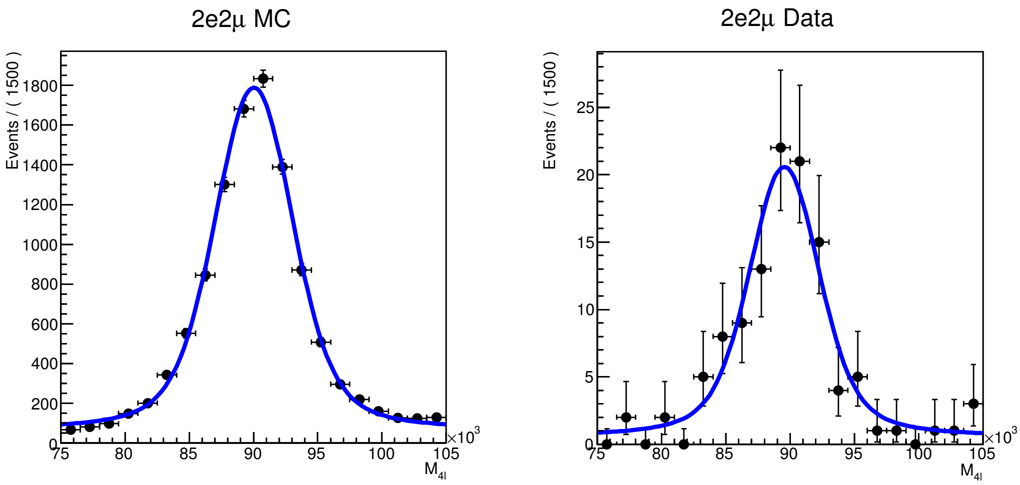

(b) Fits of the function defined in Eqn 8.2 to MC signal (left) and data (right), including a floating constant term.

Figure 8.2.: Results of the two mass fit strategies shown for the $2e2\mu$ channel.

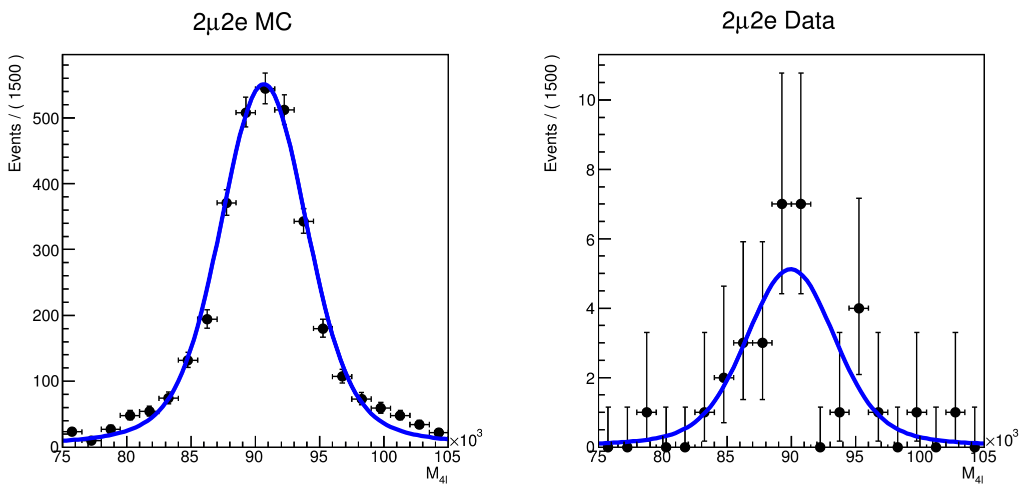

(a) Fits of the function defined in Eqn. 8.2 to MC signal (left) and data (right).

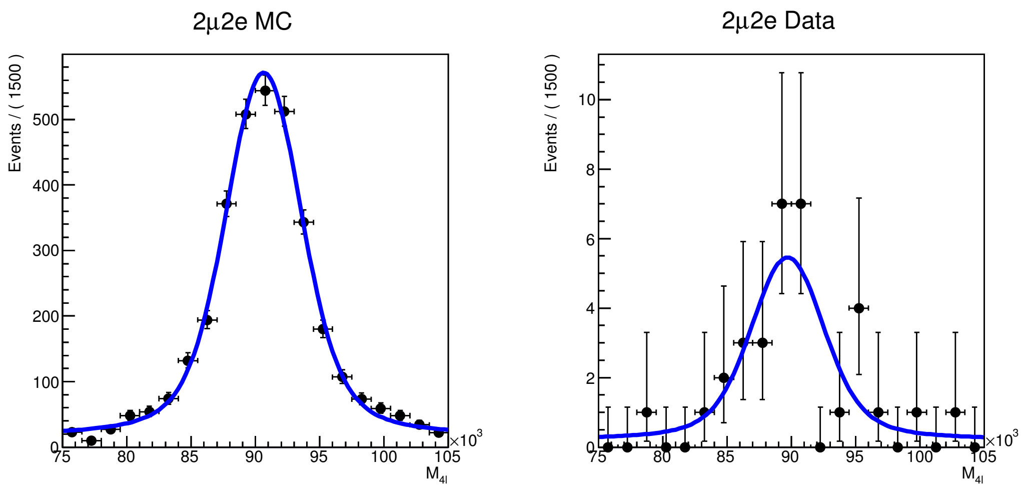

(b) Fits of the function defined in Eqn 8.2 to MC signal (left) and data (right), including a floating constant term.

Figure 8.3.: Results of the two mass fit strategies shown for the $2\mu 2e$ channel.

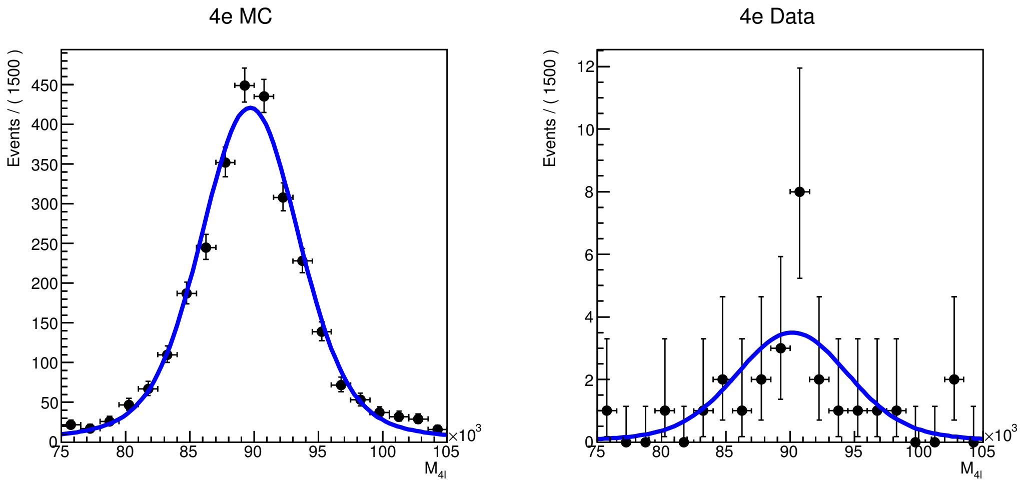

(a) Fits of the function defined in Eqn. 8.2 to MC signal (left) and data (right).

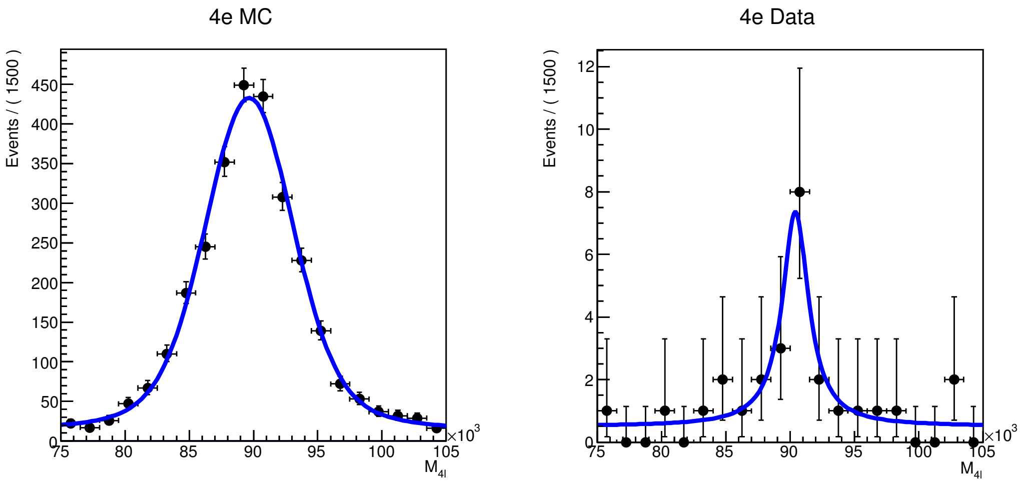

(b) Fits of the function defined in Eqn 8.2 to MC signal (left) and data (right), including a floating constant term.

Figure 8.4.: Results of the two mass fit strategies shown for the 4e channel.

Table 8.1.: Fitted mass and Gaussian resolution parameters for the function derived in Equation 8.2 with no offset term. Results are presented for both data and MC spectra, with the percent difference and significance of $\Delta M = M_{\mathrm{DATA}} - M_{\mathrm{MC}}$ included.

BW $\star$ Gaussian					
Parameter		$4e$	$2e2\mu$	$2\mu 2e$	4μ
Mass (GeV)	MC	89.68 ± 0.08	90.05 ± 0.04	90.65 ± 0.07	90.91 ± 0.03
	Data	90.2 ± 1.1	89.5 ± 0.3	90.0 ± 0.8	90.7 ± 0.3
$\|\Delta M\|$ (%)		$(0.5 \pm 1.2)\%$	$(0.6 \pm 0.4)\%$	$(0.8 \pm 0.9)\%$	$(0.3 \pm 0.4)\%$
ΔM Significance		0.5σ	-1.5σ	-0.9σ	-0.7σ
Resolution (GeV)	MC	3.27 ± 0.09	2.99 ± 0.05	3.80 ± 0.09	1.75 ± 0.04
	Data	4 ± 2	2.4 ± 0.4	2.9 ± 0.9	2.4 ± 0.4
$\Delta\sigma$ Significance		0.3σ	-1.7σ	-1.0σ	1.6σ

Table 8.2.: Fitted mass and Gaussian resolution parameters for the function derived in Equation 8.2, with a constant offset allowed to float. Results are presented for both data and MC spectra, with the percent difference and significance of $\Delta M = M_{\mathrm{DATA}} - M_{\mathrm{MC}}$ included.

BW $\star$ Gaussian + constant					
Parameter		$4e$	$2e2\mu$	$2\mu 2e$	4μ
Mass (GeV)	MC	89.67 ± 0.09	90.03 ± 0.04	90.64 ± 0.07	90.90 ± 0.03
	Data	90.4 ± 0.4	89.6 ± 0.4	89.7 ± 0.9	90.6 ± 0.3
$\|\Delta M\|$ (%)		$(0.8 \pm 0.4)\%$	$(0.5 \pm 0.4)\%$	$(1 \pm 1)\%$	$(0.4 \pm 0.4)\%$
ΔM Significance		2.0σ	-1.4σ	-1.0σ	-1.0σ
Resolution (GeV)	MC	2.9 ± 0.1	2.48 ± 0.05	2.39 ± 0.09	1.75 ± 0.04
	Data	4.9 ± 7.8	2.2 ± 0.4	2.3 ± 1.4	2.5 ± 0.4
$\Delta\sigma$ Significance		0.3σ	-0.9σ	-0.1σ	1.6σ

Chapter 9.

Conclusions

Several studies of the resonance produced by the decay of a single Z boson to four leptons have been presented, using 20.3 fb^{-1} of ATLAS data recorded in pp collisions at $\sqrt{s} = 8$ TeV. In the phase space defined by 80 GeV $< M_{4\ell} <$ 100 GeV and $M_{\ell^+\ell^-} \geq$ 4 GeV, fiducial and total cross-sections were measured in four final states ($4e$, $2e2\mu$, $2\mu 2e$, and 4μ). The combined phase space cross-section for $\text{Z} \to \ell^+\ell^-\ell^+\ell^-$ was measured as 149 ± 15 (stat.) $\pm$ 15 (syst.) $\pm$ 4 (lumi.) fb. This measurement agrees with the SM prediction of 142.2 ± 0.4 fb.

The branching ratio of the Z boson to four leptons, $BR(\text{Z} \to \ell^+\ell^-\ell^+\ell^-)$, was also measured, subtracting the contribution of t-channel diagrams from the measured phase space cross-section. The measured value of the branching ratio, $(4.6 \pm 0.6) \times 10^{-6}$, agrees with the SM prediction of $(4.50 \pm 0.03) \times 10^{-6}$. It also agrees with the value measured by CMS using $\sqrt{s} = 7$ TeV data, $(4.2^{+0.9}_{-0.8}$ (stat.) $\pm$ 0.2 (syst.)) $\times 10^{-6}$.

Motivation for extending the analysis to a more inclusive phase space defined by 80 GeV $< M_{4\ell} <$ 100 GeV and $M_{\ell^+\ell^-} \geq$ 1 GeV was discussed, and shape validation for low-mass MC samples was presented. Fiducial and total cross-section measurements for this new phase space were presented as preliminary results, in light of a discrepancy observed in signal MC normalisations at low `mllmin`.

Finally, analytical fits of the four-lepton mass distributions measured by this extended analysis were performed to cross-check the four-lepton mass scale around $M_{4\ell} \approx M_Z$. The mass scale is determined to be accurate within uncertainties.

Colophon

This thesis was made in $\LaTeX\,2_\varepsilon$ using the *hepthesis* class, written by Andy Buckley [54].

Appendix A.

Muon Track Quality Requirements

Combined+Segment-Tagged Track Requirements:

```
!expectBLayerHit || nBLHits > 0
nPixHits + nPixelDeadSensors >0
nSCTHits + nSCTDeadSensors > 4
nPixHoles + nSCTHoles < 3

n = nTRTHits + nTRTOutliers
if (0.1<|eta| < 1.9): require if n > 5 && nTRTOutliers < n*0.9
else if (|eta| < 0.1 or |eta| 1.9): if n > 5 require nTRTOutliers < n*0.9
```

Calo-Tagged Muon Track Requirements:

```
!expectBLayerHit || nBLHits > 0
nPixHits + nPixelDeadSensors > 0
nSCTHits + nSCTDeadSensors > 4
nPixHoles + nSCTHoles < 3

n = nTRTHits + nTRTOutliers
if (|eta| < 0.1): pass if n < 6 || nTRTOutliers < n*0.9
```

Bibliography

[1] ATLAS Collaboration, *Determination of the muon reconstruction efficiency in ATLAS at the Z resonance in proton-proton collisons at* $\sqrt{s} = 7$ TeV, ATLAS-CONF-2011-008.

[2] CMS Collaboration, *Measurement of the Inclusive W and Z Production Cross Sections in pp Collisions at* $\sqrt{s} = 7$ *TeV with the CMS experiment*, J. High Energy Phys. **10** (2011) 132, `arXiv:1107.4789 [hep-ex]`.

[3] ATLAS Collaboration, *Observation of a new particle in the search for the Standard Model Higgs boson with the ATLAS detector at the LHC*, Phys. Lett. B **716** no. 1, (2012) 1–29, `arXiv:1207.7214 [hep-ex]`.

[4] CMS Collaboration, *Observation of a new boson at a mass of 125 GeV with the CMS experiment at the LHC*, Phys. Lett. B **716** no. 1, (2012) 30–61, `arXiv:1207.7235 [hep-ex]`.

[5] ATLAS Collaboration, *Measurements of the properties of the Higgs-like boson in the four lepton decay channel with the ATLAS detector using 25 fb*$^{-1}$ *of proton-proton collision data*, ATLAS-CONF-2013-013.

[6] CMS Collaboration, *Properties of the Higgs-like boson in the decay H to ZZ to 4*ℓ *in pp collisions at* $\sqrt{s} = 7$ *and 8 TeV*, CMS-PAS-HIG-13-002.

[7] ATLAS Collaboration, *ATLAS measurements of the 7 and 8 TeV cross sections for* $Z \rightarrow 4\ell$ *in pp collisions*, ATLAS-CONF-2013-055.

[8] CMS Collaboration, *Observation of Z decays to four leptons with the CMS detector at the LHC*, J. High Energy Phys. **2012** no. 12, (2012) 1–28, `arXiv:1210.3844 [hep-ex]`.

[9] ATLAS Collaboration, *Measurement of the total ZZ production cross section in proton-proton collisions at* $\sqrt{s} = 8$ TeV *in 20 fb*$^{-1}$ *with the ATLAS detector*, ATLAS-CONF-2013-020.

[10] S. Alioli, P. Nason, C. Oleari, and E. Re, *A general framework for implementing NLO calculations in shower Monte Carlo programs: the POWHEG BOX*, J. High Energy Phys. **06** (2010) 043, arXiv:1002.2581 [hep-ph].

[11] P. Nason, *A New Method for Combining NLO QCD with Shower Monte Carlo Algorithms*, J. High Energy Phys. **0411** (2004) 040, arXiv:hep-ph/0409146.

[12] S. Frixione, P. Nason, and C. Oleari, *Matching NLO QCD computations with parton shower simulations: the POWHEG method*, J. High Energy Phys. **11** (2007) 070, arXiv:0709.2092 [hep-ph].

[13] L. Evans and P. Bryant, *LHC Machine*, J. Instrum. **3** no. 8, (2008) S08001.

[14] ATLAS Collaboration, *The ATLAS experiment at the CERN Large Hadron Collider*, J. Instrum. **3** (2008) S08003.

[15] ATLAS Collaboration, *The ATLAS Inner Detector commissioning and calibration*, Eur. Phys. J. C **70** (2010) 787–821, arXiv:1004.5293 [ins-det].

[16] ATLAS Collaboration, *Readiness of the ATLAS Liquid Argon Calorimeter for LHC Collisions*, Eur. Phys. J. C **70** (2010) 723–753, arXiv:0912.2642 [ins-det].

[17] ATLAS Collaboration, *Commissioning of the ATLAS Muon Spectrometer with Cosmic Rays*, Eur. Phys. J. C **70** (2010) 875–916, arXiv:1006.4384 [ins-det].

[18] ATLAS Collaboration, *Performance of the ATLAS trigger system in 2010*, Eur. Phys. J. C **72** no. 1849, (2012) 1849, arXiv:1110.1530 [hep-ex].

[19] S. Ballestrero, W. Vandelli, and G. Avolio, *ATLAS TDAQ system: current status and performance*, ATL-DAQ-PROC-2011-020.

[20] ATLAS Collaboration, *Performance of the ATLAS Electron and Photon Trigger in p-p Collisions at $\sqrt{s} = 7$ TeV in 2011*, ATLAS-CONF-2012-048.

[21] ATLAS Collaboration, *Performance of the ATLAS muon trigger in 2011*, ATLAS-CONF-2012-099.

[22] T. Melia, P. Nason, R. Rontsch, and G. Zanderighi, *W^+W^-, WZ and ZZ production in the POWHEG BOX*, J. High Energy Phys. **11** (2011) 078, arXiv:1107.5051 [hep-ph].

[23] T. Gleisberg, S. Hoeche, F. Krauss, M. Schonherr, S. Schumann, et al., *Event generation with SHERPA 1.1*, J. High Energy Phys. **02** (2009) 007, arXiv:0811.4622 [hep-ph].

[24] M. L. Mangano, F. Piccinini, A. D. Polosa, M. Moretti, and R. Pittau, *ALPGEN, a generator for hard multiparton processes in hadronic collisions*, J. High Energy Phys. **0307** (2003) 001, `arXiv:hep-ph/0206293`.

[25] S. Frixione and B. R. Webber, *Matching NLO QCD computations and parton shower simulations*, J. High Energy Phys. **06** (2002) 029, `arXiv:hep-ph/0204244`.

[26] S. Jadach, Z. Was, R. Decker, and J. H. Kuhn, *The tau decay library TAUOLA: Version 2.4*, Comput. Phys. Commun. **76** (1993) 361–380.

[27] P. Golonka et al., *The tauola-photos-F environment for the TAUOLA and PHOTOS packages, release II*, Comput. Phys. Commun. **174** (2006) 818–835, `arXiv:hep-ph/0312240`.

[28] P. Golonka and Z. Was, *PHOTOS Monte Carlo: a precision tool for QED corrections in Z and W decays*, Eur. Phys. J. C **45** (2006) 97–107, `arXiv:hep-ph/0506026`.

[29] N. Davidson, T. Przedzinski, and Z. Was, *PHOTOS interface in C++: technical and physics documentation*, `arXiv:1011.0937 [hep-ph]`.

[30] T. Sjostrand, S. Mrenna, and P. Z. Skands, *A brief introduction to PYTHIA 8.1*, Comput. Phys. Commun. **178** (2008) 852–867, `arXiv:0710.3820 [hep-ph]`.

[31] J. M. Butterworth, J. R. Forshaw, and M. H. Seymour, *Multiparton interactions in photoproduction at HERA*, Z. Phys. C Part. Fields **72** (1996) 637–646, `arXiv:hep-ph/9601371`.

[32] J. Pumplin et al., *New generation of parton distributions with uncertainties from global QCD analysis*, J. High Energy Phys. **07** (2002) 012, `arXiv:hep-ph/0201195`.

[33] H.-L. Lai et al., *New parton distributions for collider physics*, Phys. Rev. D **82** (2010) 074024, `arXiv:1007.2241 [hep-ph]`.

[34] ATLAS Collaboration, *Summary of ATLAS Pythia 8 tunes*, ATL-PHYS-PUB-2012-003.

[35] ATLAS Collaboration, *The ATLAS Simulation Infrastructure*, Eur. Phys. J. C **70** (2010) 823–874, `arXiv:1005.4568 [ins-det]`.

[36] GEANT4 Collaboration, S. Agostinelli et al., *GEANT4: A simulation toolkit*, Nucl. Instrum. Meth. A **A506** (2003) 250–303.

[37] ATLAS Collaboration, *Multiple Year Collision Plots*, 2012. `https://twiki.cern.ch/twiki/bin/view/AtlasPublic/LuminosityPublicResults/`.

[38] T. Golling, H. Hayward, P. Onyisi, H. Stelzer, and P. Waller, *The ATLAS data quality defect database system*, Eur. Phys. J C **72** no. 4, (2012) 1–6.

[39] J. Adelman, M. Baak, N. Boelaert, M. D'Onofrio, J. A. Frost, C. Guyot, M. Hauschild, A. Hoecker, K. J. C. Leney, E. Lytken, M. Martinez-Perez, J. Masik, A. M. Nairz, P. U. E. Onyisi, S. Roe, S. Schaetzel, and M. G. Wilson, *ATLAS offline data quality monitoring*, J. Phys.: Conf. Ser. **219** no. 4, (2010) 042018.

[40] W. Lampl, S. Laplace, D. Lelas, P. Loch, H. Ma, S. Menke, S. Rajagopalan, D. Rousseau, S. Snyder, and G. Unal, *Calorimeter Clustering Algorithms: Description and Performance*, ATL-LARG-PUB-2008-002.

[41] ATLAS Collaboration, *Improved electron reconstruction in ATLAS using the gaussian sum filter-based model for bremsstrahlung*, ATLAS-CONF-2012-047.

[42] ATLAS Collaboration, *Electron performance measurements with the ATLAS detector using the 2010 LHC proton-proton collision data*, Eur. Phys. J. C **72** (2012) 1909, `arXiv:1110.3174 [hep-ex]`.

[43] ATLAS Collaboration, *Muon reconstruction efficiency in reprocessed 2010 LHC proton-proton collision data recorded with the ATLAS detector*, ATLAS-CONF-2011-063.

[44] ATLAS Collaboration, *A measurement of the muon reconstruction efficiency in 2010 ATLAS data using J/ψ decays*, ATLAS-CONF-2012-125.

[45] ATLAS Collaboration, *Muon Momentum Resolution in First Pass Reconstruction of pp Collision Data Recorded by ATLAS in 2010*, ATLAS-CONF-2011-046.

[46] ATLAS Collaboration, *Preliminary results on the muon reconstruction efficiency, momentum resolution, and momentum scale in ATLAS 2012 pp collision data*, ATLAS-CONF-2013-088.

[47] J. P. Ottersbach, *Muons in early ATLAS data: from first collisions to W^+W^- production.* PhD thesis, NIKHEF, 2012.

[48] ATLAS Collaboration, *Updated results and measurements of properties of the new Higgs-like particle in the four-lepton decay channel with the ATLAS detector*, ATLAS-CONF-2012-169.

[49] S. van der Meer, *Calibration of the effective beam height in the ISR*, CERN-ISR-PO-68-31.

[50] ATLAS Collaboration, *Luminosity Determination in pp Collisions at* $\sqrt{s} = 7$ TeV *Using the ATLAS Detector at the LHC*, Eur. Phys. J. C **71** (2011) 16–30, `arXiv:1101.2185 [hep-ex]`.

[51] P. Renton, *Electroweak Interactions: An Introduction to the Physics of Quarks and Leptons.* Cambridge University Press, 1990.

[52] Particle Data Group Collaboration, J. Beringer et al., *Review of Particle Physics*, Phys. Rev. D **86** (2012) 010001.

[53] W. Verkerke and D. Kirkby, *The RooFit toolkit for data modeling*, `arXiv:physics/0306116 [data-an]`.

[54] A. Buckley, *The hepthesis LaTeX package*, CTAN. `http://www.ctan.org/pkg/hepthesis`.